

## AIRBORNE GRAVITY GRADIOMETRY – DATA PROCESSING AND INTERPRETATION

Dionisio Uendro Carlos, Marco Antonio Braga, Henry F. Galbiatti and Wanderson Roberto Pereira

**ABSTRACT.** This paper discusses some processing techniques (all codes were implemented with open source software) developed for airborne gravity gradient systems, aiming at outlining geological features by applying mathematical formulations based on the potential field properties and its breakdown into gradiometric tensors. These techniques were applied to both synthetic and real data. These techniques applied to synthetic data allow working in a controlled environment, understanding the different processing results and establishing a comparative parameter. These methodologies were applied to a survey area of the *Quadrilátero Ferrífero* to map iron ore targets, resulting in a set of very helpful and important information for geological mapping activities and *a priori* information for inversion geophysical models.

**Keywords:** processing, airborne gravity gradiometry, iron ore exploration, FTG system, FALCON system.

**RESUMO.** Neste trabalho apresentamos algumas técnicas de processamento (todos os códigos foram implementados em softwares livres) desenvolvidas para aplicação aos dados de aerogravimetria gravimétrica. Os processamentos foram aplicados tanto a dados sintéticos como a dados reais. A aplicação a dados sintéticos permite atuar em um ambiente controlado e entender o padrão resultante de cada processamento. Esses mesmos processamentos foram aplicados em uma área do Quadrilátero Ferrífero para o mapeamento de minério de ferro. Todos os resultados desses processamentos são muito úteis e importantes para o mapeamento geológico e como informação *a priori* para modelos de inversão geofísica.

**Palavras-chave:** processamento, dados de aerogravimetria gravimétrica, exploração de minério de ferro, sistema FTG, sistema FALCON.

## INTRODUCTION

Most major practical advances in geophysical exploration are linked to oil exploration due to the large amount of resources available to invest in innovation for the development of new technologies. Within this context occurs the advent of a technology capable to collect a huge amount of data, in relatively short time, which is originated in this segment of exploration geophysics as consequence of the necessity to create a system of a moving and stable platform, carrying multiple gravimeters. From this analysis arise the first deepwater gravity meters that were used to locate salt domes in the Gulf of Mexico before the seismic surveys (Braga, 2009). The use of gravimeters in mobile platform led to the improvement of the use of gradiometers.

In the early 1970s, the National Aeronautics and Space Administration (North American Space Agency – NASA) initiated the development of scientific programs to demonstrate the feasibility of measuring the mass distribution of the Earth, the Moon and other celestial bodies by the detection of spatial gradients from the field of orbital vehicles using a rotating gravity gradiometer (Bell, 1971). In the same decade, during the Cold War, where both American and Russian navies realized that accuracy of launching ballistic missiles from submarines (SLBM's) relied heavily on the precise knowledge of gravity during the entire trajectory in time for launching the missile (Rogers, 2009).

In the mid-1970s, there were three different types of gradiometers (Hopkins, 1975). The gradiometer operated by Bell Geospace Company<sup>1</sup> (Metzger, 1974 *apud* Hopkins, 1975) consisted of four accelerometers mounted on a rotating support. Two diagonal terms of the gradient tensor and their cross terms are derived from linear combinations of acceleration measurements. The Hughes Research Laboratories (Ames et al., 1973 *apud* Hopkins, 1975) developed an instrument that used mass bodies mounted in pairs of pivotable arms. The gravity gradient supplied the torque on each pivotable arm which was measured at the bending point by a sensor. Again, two diagonal terms and their cross terms were derived from the output of their sensors. The third gradiometer of at that time was from Charles Stark Draper Laboratory (Trageser & Johnson, 1974 *apud* Hopkins, 1975), which used a floating spherical support of a pair of test masses. In this configuration the gravity gradient induces a slight rotation in the floating mass, which is measured by a capacitor.

Two diagonal terms of the gravity tensor are derived from the instrument output.

From the several prototypes of gravity gradiometers developed in the 1970s (Trageser, 1970; Metzger, 1977; Forward, 1981), the United States Navy has selected the Gravity Sensors System (GGS) from the Bell Aerospace Company to offset the gravity of its inertial navigation systems (Dransfield, 2007). In the early 1980s, Bell Aerospace Textron<sup>2</sup> developed a mobile base gravimetric gradiometer tensor system for the U.S. Navy. This instrument, developed by Ernest Metzger costing 400 million dollars to develop and was selected by the US Navy as a requirement of the inertial navigation system for submarine Trident (Rogers, 2009).

In 1983, the Air Force Geophysics Laboratory (AFGL) selected the same gravity gradiometer for the Defense Mapping Agency (DMA) proposing a program of regional gravity mapping (Jekeli, 1988 *apud* Dransfield, 2007). It is an important timeline because only after the opening of the Navy system technology is that the Air Force could use this system, called Gravity Gradiometer Survey System (GGSS), see Figures 1A to 1E.

According to Dransfield (2007), the system that was developed by the Geophysical Laboratory of the Air Force became the future platform for the 3D-FTG system. The first airborne test of the system took place in 1988. The entire system, which was mounted on a van (Winnebago), was installed in a Hercules C-130 aircraft (Fig. 1E).

This system flew over a test area in Oklahoma Texas Panhandle. The GGSS performance was limited due to problems of the Global Positioning System – GPS, gyroscope and temperature control. More serious problems were observed with the Gravity Gradients Instruments<sup>3</sup> due to the acceleration changing in the aircraft (Pfohl et al., 1988 *apud* Dransfield, 2007). The final test was performed to demonstrate the efficiency and accuracy of the gravity vector map along rail lines to support a mobile missile system. The tests were conducted early 1989 in the states of Colorado, Kansas and New Mexico. However, despite of not being reported in the literature, a qualitative study of the data was presented by Brzezowski et al. (1990) *apud* Jekeli (1993).

Then we finally reached the current systems that are used for geological surveys. Companies that operate commercial systems are: Bell Geospace (3D-FTG), ARKeX (FTGeX), GEDEX (HD-AGG)<sup>4</sup> and FUGRO (AGG-Falcon), Rogers (2009). We will

<sup>1</sup> Often confused with Bell Geospace, the current owner of the 3D-FTG system.

<sup>2</sup> Currently Lockheed Martin.

<sup>3</sup> GGI's for convenience.

<sup>4</sup> It is a new system based on the superconductor concept and, therefore, different from the worldwide known systems: 3D-FTG by the Bell Geospace and AGG Falcon by Fugro.

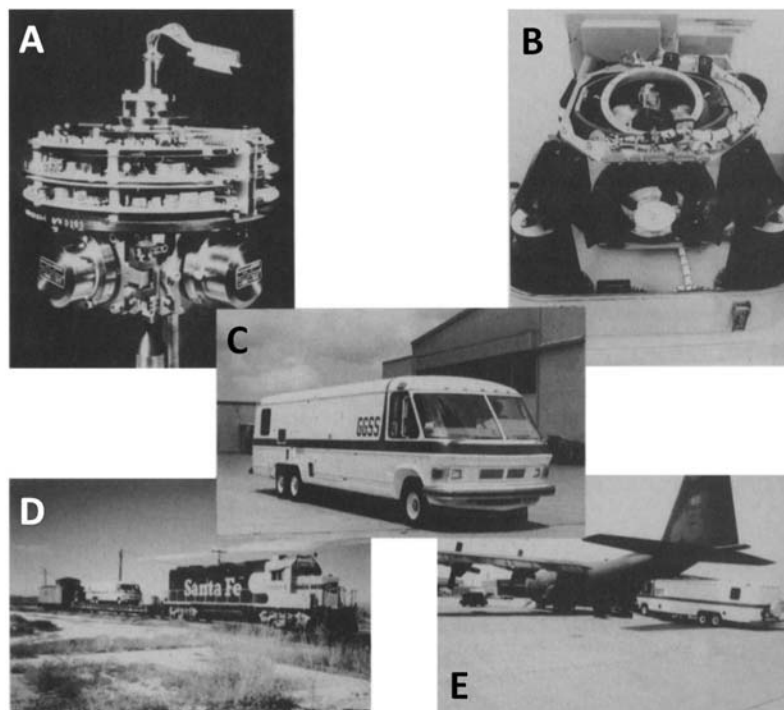


**Figure 1** – The main components and mechanisms of GGSS. (A) Gravity Gradiometer Instrument (two accelerometers are visible). (B) Carousel platform. (C) The van where the GGSS platform and support were mounted. (D) The system mounted on the van being transported via railway. (E) The van being loaded aboard the C-130 Hercules aircraft from the U.S. Air Force. Adapted from Jekeli (1993).

give more details on the two systems that were used in this work: 3D-FTG and Falcon.

### GRAVITY GRADIENT ROTATING ACCELEROMETER

The two systems presented in this work, the 3D-FTG and Falcon are made up of gravity gradient rotating accelerometers. It is important to note that in the 3D-FTG system all the components of the gravity gradient tensor are acquired (actually due to redundancy, for example  $G_{xy} = G_{yx}$ , etc., and the fact that  $G_{zz} = -(G_{xx} + G_{yy})$  we end up with five independent components) while in the Falcon system only two components,  $G_{xz}$  and  $G_{UV}$ , are measured and subsequently used to calculate  $G_{zz}$ <sup>5</sup>. Figure 2 is a representation of this type of gradiometer.

### 3D-FTG

When viewed externally, the 3D-FTG system consists basically of two parts: an aviation capsule and the electronic rack. The aviation capsule measures about 1 m<sup>3</sup> and weighs approximately 227 kg

with installed GGIs. The main function of the aviation capsule is to keep controlled the temperature, pressure and humidity. The electronic rack has the same dimensions of the aviation capsule and weighs 160 kg (Braga et al., 2009).

Each Gravity Gradient Instrument (GGI) is made up of accelerometers which are mounted internally on a disc that rotates at a certain angular velocity. In the 3D FTG system, the GGI's are arranged in an umbrella-like geometry as shown in Figure 3. In each GGI of Figure 3, four accelerometers are mounted internally on each of the rotating disks.

### Falcon

Simultaneously to the development of the 3D-FTG system the Anglo-Australian BHP Billiton<sup>6</sup> signed a contract with Lockheed Martin to develop a gravity gradiometer especially designed for airborne use (AGG, or Airborne Gravity Gradiometer), Dransfield (2007). The Falcon system was considered the first airborne gravity gradiometer, tested in 1997 and used for an airborne

<sup>5</sup>Commercially, the components of the 3D-FTG system are represented by an uppercase *T* for Tensor followed by the subscript *x*, *y* or *z*. Also, *x* = 1, *y* = 2 and *z* = 3 can be used. The AGG system (Airborne Gravity Gradiometer) Falcon uses uppercase *G* for Gradient followed by the subscript: *x* = *N* (Northing), *y* = *E* (Easting) and *z* = *D* (Down).

<sup>6</sup>In 2007, BHP Billiton sold its system to FUGRO.

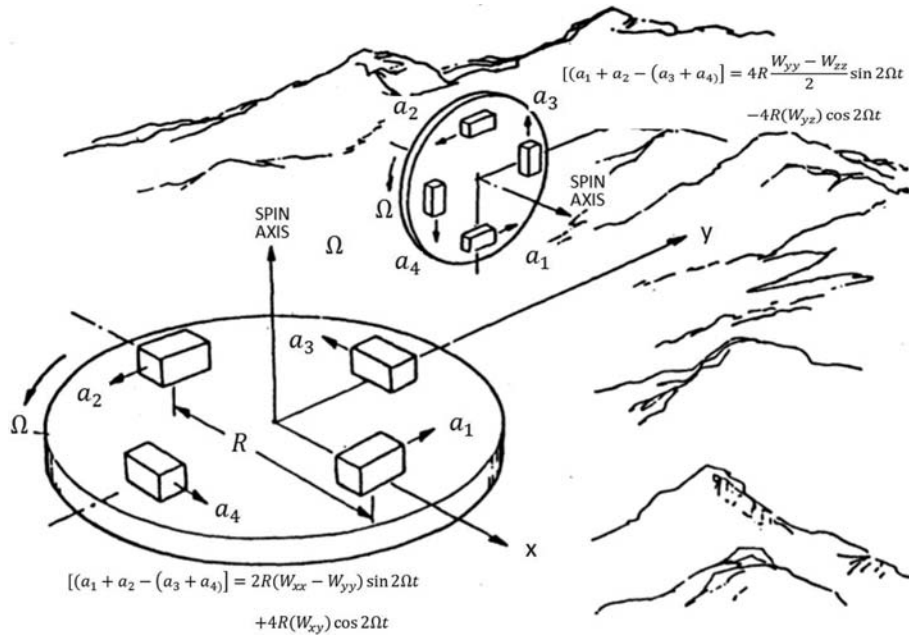


Figure 2 – Representation of rotational accelerometers gravity gradient according to Metzger (1986).

survey in 1999. Unlike the 3D-FTG system, that measures five components of tensor gravity, the Falcon system measures two components,  $G_{NE}$  ( $T_{xy}$  or  $G_{xy}$ ) and  $G_{UV}$  ( $W_{delta}$ ) – (curvature) – and the  $G_{DD}$  ( $T_{zz}$  or  $G_{zz}$ ) component is calculated using these two components.

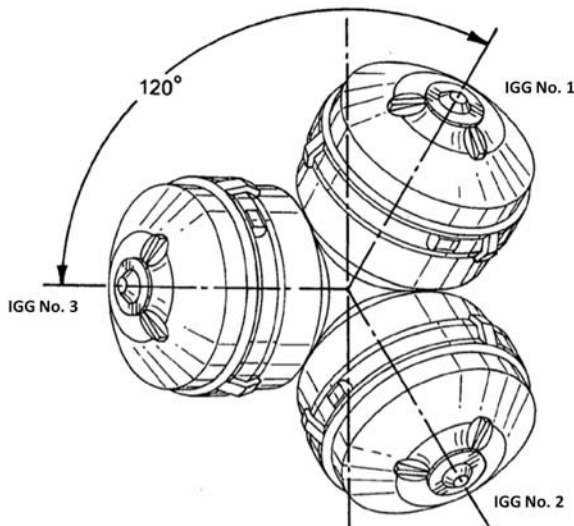


Figure 3 – Umbrella-like arrangement of Gravity Gradient Instruments (GGI) according to Brett & Brewster (2010).

The noise of the vertical gravity gradient achieves about 5 Eötvös (E) after post-processing techniques similar to those used by the Bell Geospace 3D-FTG system. In addition, the system uses a Falcon Butterworth 400-meter wavelength filter (Dransfield

et al., 2001; Lane, 2004 *apud* Rogers, 2009). Unlike the 3D-FTG or Air-FTG system, the Falcon system consists of a single GGI module measuring approximately two length units related to the dimensions of a single GGI of the 3D FTG system (Galbiatti et al., 2011).

The main source of measurable noise is the motion sensitivity of the GGI. The magnitude of the signal of the gravity gradient expected for a mineral deposit varies from 1 E to 100 E. The accelerations experienced by an aircraft during low altitude flights are approximately 1-10 m/s<sup>2</sup>. The acceleration rejection of a GGI is of the order of 10<sup>-9</sup> (O’Keefe et al., 1999). Likewise the 3D-FTG system, the Falcon system consists of an aviation capsule and an electronic rack.

### PRE-PROCESSING OF GRAVIMETRIC GRADIOMETRIC DATA

The two systems have different pre-processing steps due to the different configurations of the gravity gradient instrument. Unfortunately the confidentiality agreements each of the owning companies has with the system’s manufacturer only a general configuration will be presented these systems.

In general, starting by the 3D-FTG system the main processing steps are: compensation, terrain correction, flight line correction and leveling. Despite of taking all precautions pertaining to operation of the equipment and aircraft during the flight a nonlin-

ear behavior occurs due to aircraft accelerations and the noise of the rotating disk. This noise is not only a direct measurement of the aircraft motion accelerations, but a sum of several accelerations onboard and to the nonlinear coefficients of accelerometers (Rogers, 2009).

To solve this problem Bell Geospace developed a procedure not described in detail in the literature, in which the aircraft acceleration and noise can be determined and eliminated. This procedure is known as High Rate Post Mission Compensation (HRPMC). This technique has been adequate for aircraft accelerations with standard deviation close to 10% of  $g$  (gravitational acceleration). Two other factors which may introduce noise to the measurements are: the misalignment of the accelerometers in each GGI combination with respect to the rotation plane and any difference in the scale factor between two opposing accelerometers, which are identified by pre-flight calibration techniques on the ground.

Gravity gradients measurements are extremely sensitive to changes in the gravitational field caused by different mass distributions. An example is the significant aircraft mass that needs to be eliminated from the acquired data. This process is performed flying over areas known as standard survey areas. The gravity gradiometer surveys follow an orthogonal pattern that results in many intersection points. Data from these intersection points are used to remove the gravitational effects of the aircraft in a process known as Low Rate Post Mission Compensation (LRPM), (Brett, 2008 *apud* Rogers, 2009).

A very important reference on the method resolution is presented by Rogers (2009). The current resolution of the 3D-FTG system after HRPMC procedures and pre-flight calibration is approximately 5 E for 1 Hz acquisition rate with a spatial resolution of a few hundred meters. Without applying the above procedures the noise levels reach approximately 12-15 E range (Murph, 2004; Brett, 2008 *apud* Rogers, 2009), almost three times the method resolution. Considering that a mineral deposit is obviously dependent on a few variables (geometry, depth, density of host rocks, etc.), it is assumed that in a density contrast of 5 E the geophysical signature becomes invisible without application of proper procedures for compensation/correction.

The terrain correction is calculated by approximating its geometry to that of tridimensional prisms. For each prism, a density of  $1.0 \text{ g/cm}^3$  is assigned and the response of each gravity gradient of a model that represents the mass of Earth between the land surface and the reference ellipsoid is calculated. Terrain corrections are calculated for each tensor component and subtracted from the observed data.

This correction can be applied to any desired density, using Equation (1).

$$\Gamma_{\alpha\beta}^{TC} = \Gamma_{\alpha\beta}^{OBS} - \rho \cdot \Gamma_{\alpha\beta}^{1g/cm^3} \quad (1)$$

where:

- $\alpha, \beta = N$  (Northing), E (Easting) and D (Down) directions;
- $\rho$  is the desired density;
- $\Gamma_{\alpha\beta}^{TC}$  tensor component already corrected by each of the  $\Gamma_{\alpha\beta}$  components with the desired density  $\rho$ ;
- $\Gamma_{\alpha\beta}^{OBS}$  is the observed ( $\Gamma_{\alpha\beta}$ ) component;
- $\Gamma_{\alpha\beta}^{1g/cm^3}$  is the terrain correction for each ( $\Gamma_{\alpha\beta}$ ) component calculated for the  $1.0 \text{ g/cm}^3$  density.

The next step is to correct the lines. This process calculates the tensor components from the GGIs in-line and cross-line outputs and removes the errors along the line. This process assumes that there is no correlation between the signal to be removed and the signal that remains (Bell Geospace, 2005). The final step is leveling the flight lines using the traditional leveling methodologies of geophysical data.

Dransfield & Gama (2010) presented the processing steps (or pre-processing) of data acquired by the Falcon system. According to these authors the main processing steps are:

1. Dynamic correction of residual aircraft motion (Post-Mission Compensation or PMC) is calculated and applied. The data are demodulated, filtered and leveled by a simple average. The output is the gravity gradient curvature,  $G_{NE}$  and  $G_{UV}$ ;
2. Auto-gradient corrections are calculated and applied to reduce the variable gradients generated by the platform and aircraft;
3. A Digital Terrain Model (DTM) is generated from the laser scanner scanning the rotational inertial navigation data from the AGG system and differential GPS data. Data from the Shuttle Radar Topography Mission (SRTM) can be used to complement the DTM generated by the laser scanner;
4. Terrain corrections are calculated from the final digital terrain model and applied to the curvature gradients  $G_{NE}$  and  $G_{UV}$ ;
5. The gradients  $G_{NE}$  and  $G_{UV}$  are leveled and processed into the full tensor gravity gradient in  $G_{DD}$  and  $g_D$ .
6. The gravity  $g_D$  is adjusted with the regional gravity.

**PROCESSING AND INTERPRETATION OF GRAVIMETRIC GRADIOMETER DATA**

Pedersen & Rasmussen (1990) and FitzGerald & Holstein (2005, 2006) published important papers that addressed specific techniques to treat potential data, especially gradient tensor data (gravity or magnetic gradiometry).

The first one developed a methodology to calculate eigenvalues, invariant and direction of the strike that were subsequently implemented in the paper of FitzGerald & Holstein (2005, 2006). The processes include:

1. Tensor Trace or Invariant 0 ( $I_0$ );
2. First Invariant ( $I_1$ );
3. Determinant ( $R_2$ );
4. Eigenvalues ( $\lambda_1, \lambda_2$  and  $\lambda_3$ );
5. Invariants 1 and 2 ratio;
6. Strike ( $\arctan(I_2/I_1)$ ).

The second paper presented possibilities to process the data as tensorial way, keeping the relationship between all the components of the gravity gradient tensor and not just working in an isolated way with each of the components. Based on this latest information FitzGerald and Holstein (2005, 2006) presented an innovative method to process data from airborne surveys, whether gravimetric or magnetic gradiometer. The main tools developed in GUI environment related to tensorial data were:

1. mimes graphs, such as the Mohr diagram for integrated visualization of all components of the gravity gradient tensor;
2. interpolation by implementing an algorithm taking into account the eigenvalues associated with the *quaternions*<sup>7</sup> of the tensor;
3. corrections of the gravity gradients, such as compensation of mobile platform and terrain correction;
4. Profile visualization represented by the tensor eigenvalues and rotations.

**Gradient Tensor Properties**

The gravitational acceleration is defined as the gradient of the gravitational potential (Equation 2):

$$g(\vec{x}) = \nabla \phi(\vec{x}) \tag{2}$$

The gravity gradient tensor is given by (Equation 3):

$$\begin{aligned} \bar{\Gamma}(\vec{x}) &= \begin{pmatrix} \bar{\Gamma}_{1,1} & \bar{\Gamma}_{1,2} & \bar{\Gamma}_{1,3} \\ \bar{\Gamma}_{2,1} & \bar{\Gamma}_{2,2} & \bar{\Gamma}_{2,3} \\ \bar{\Gamma}_{3,1} & \bar{\Gamma}_{3,2} & \bar{\Gamma}_{3,3} \end{pmatrix} \\ &= \nabla \nabla^T \phi(\vec{x}) = \begin{pmatrix} \frac{\partial g_1}{\partial x_1} & \frac{\partial g_2}{\partial x_1} & \frac{\partial g_3}{\partial x_1} \\ \frac{\partial g_1}{\partial x_2} & \frac{\partial g_2}{\partial x_2} & \frac{\partial g_3}{\partial x_2} \\ \frac{\partial g_1}{\partial x_3} & \frac{\partial g_2}{\partial x_3} & \frac{\partial g_3}{\partial x_3} \end{pmatrix} \end{aligned} \tag{3}$$

The diagonal contains the in-line components while outside the diagonal are the cross-gradients.

The trace of the gradient tensor is Invariant Zero<sup>8</sup>. The determinant  $\bar{\Gamma}$  (Invariant 1) and the sum of the determinants of the secondary diagonal (Invariant 2) are also invariant. These invariants can be collected as generalized determinants of rank 1, 2 and 3 (Dransfield, 1994 *apud* Jekeli, 2006):

$$D_1 \bar{\Gamma}(\vec{x}) = I_0 = \bar{\Gamma}_{1,1} + \bar{\Gamma}_{2,2} + \bar{\Gamma}_{3,3} \tag{4}$$

$$\begin{aligned} D_1 \bar{\Gamma}(\vec{x}) = I_1 &= \begin{vmatrix} \bar{\Gamma}_{1,1} & \bar{\Gamma}_{1,2} \\ \bar{\Gamma}_{2,1} & \bar{\Gamma}_{2,2} \end{vmatrix} + \begin{vmatrix} \bar{\Gamma}_{2,2} & \bar{\Gamma}_{2,3} \\ \bar{\Gamma}_{3,2} & \bar{\Gamma}_{3,3} \end{vmatrix} \\ &+ \begin{vmatrix} \bar{\Gamma}_{3,3} & \bar{\Gamma}_{3,1} \\ \bar{\Gamma}_{1,3} & \bar{\Gamma}_{1,1} \end{vmatrix} \end{aligned} \tag{5}$$

$$D_3 \bar{\Gamma}(\vec{x}) = I_2 = \begin{vmatrix} \bar{\Gamma}_{1,1} & \bar{\Gamma}_{1,2} & \bar{\Gamma}_{1,3} \\ \bar{\Gamma}_{2,1} & \bar{\Gamma}_{2,2} & \bar{\Gamma}_{2,3} \\ \bar{\Gamma}_{3,1} & \bar{\Gamma}_{3,2} & \bar{\Gamma}_{3,3} \end{vmatrix} \tag{6}$$

From equation (3), the symmetric matrix  $\Gamma$  can be “diagonalized” with real eigenvalues while the eigenvectors can be written as (Pedersen & Rasmussen, 1990):

$$\vec{V} = [\nu_1 \nu_2 \nu_3] \tag{7}$$

And the eigenvalues as:

$$\vec{\Lambda} = \begin{bmatrix} \lambda_1 & 0 & 0 \\ 0 & \lambda_2 & 0 \\ 0 & 0 & \lambda_3 \end{bmatrix} \tag{8}$$

Therefore,  $\Gamma$  can be reduced to a diagonal form  $\Lambda$  by a coordinate transformation:

$$\vec{V}^T \bar{\Gamma} \vec{V} = \bar{\Lambda} \tag{9}$$

<sup>7</sup>Generalization of the complex number:  $a + xi + yj + zk$ , where  $a, x, y$  and  $z$  are the real numbers and  $i, j, k$ , imaginary numbers.

<sup>8</sup>The terminology adopted is Invariants ( $I_0, I_1$  and  $I_2$ ), as in Pedersen & Rasmussen (1990).

On any coordinate transformation  $\Gamma$  contains three invariants (Pedersen & Rasmussen, 1990; Beiki & Pedersen, 2010):

$$I_0 = \text{trace}(\bar{\Gamma}) = \sum_{i=1}^3 \Gamma_{ii} = 0 \tag{10}$$

$$I_1 = \Gamma_{11}\Gamma_{22} + \Gamma_{22}\Gamma_{33} + \Gamma_{11}\Gamma_{33} - \Gamma_{12}^2 - \Gamma_{23}^2 - \Gamma_{13}^2 = \lambda_1\lambda_2 + \lambda_2\lambda_3 + \lambda_1\lambda_3 \tag{11}$$

$$I_2 = \det(\bar{\Gamma}) = \Gamma_{11}(\Gamma_{22}\Gamma_{33} - \Gamma_{23}^2) - \Gamma_{12}(\Gamma_{23}\Gamma_{13} - \Gamma_{12}\Gamma_{33}) + \Gamma_{13}(\Gamma_{12}\Gamma_{23} - \Gamma_{13}\Gamma_{22}) = \lambda_1\lambda_2\lambda_3 \tag{12}$$

where the indices 1, 2 and 3 illustrate the coordinate systems of the 3D-FTG data, that is,  $x = 1, y = 2$  and  $z = 3$  or data Falcon,  $N = 1, E = 2, D = 3$ . As can be seen from equation (10) is the trace of the tensor representation of Laplace's equation, or the main diagonal.

The characteristic equation for the eigenvalues is:

$$\lambda^3 - I_0\lambda^2 + I_1\lambda - I_2 = \lambda^3 + I_1\lambda - I_2 = 0 \tag{13}$$

Equation (13) has the following roots:

$$\begin{aligned} \lambda_1 &= C + D \\ \lambda_2 &= -\frac{C + D}{2} + \frac{C - D}{2}\sqrt{-3} \\ \lambda_3 &= -\frac{C + D}{2} - \frac{C - D}{2}\sqrt{-3} \end{aligned} \tag{14}$$

where:

$$C = \sqrt[3]{\frac{I_2}{2} + \sqrt{\left[\left(\frac{I_2}{2}\right)^2 + \left(\frac{I_1}{3}\right)^3\right]} } \tag{15}$$

$$D = \sqrt[3]{\frac{I_2}{2} - \sqrt{\left[\left(\frac{I_2}{2}\right)^2 + \left(\frac{I_1}{3}\right)^3\right]} } \tag{16}$$

The assumption that all  $\lambda$  are real leads the following link for the gradient tensor ( $I_2/I_1$  ratio):

$$0 \leq I \equiv -\frac{\left(\frac{I_2}{2}\right)^2}{\left(\frac{I_1}{3}\right)^3} \leq 1 \tag{17}$$

According to Pedersen & Rasmussen (1990),  $I$  shall be zero if the field is invariant along a certain direction, which means that the body causing the fault is bi-dimensional.  $I$  is equal to 1 for a monopole.

An important relationship that applies to gravity gradiometer data for analysis of geological structures is the strike direction (Murph & Brewster, 2007; Dickinson et al., 2010). Details of the development of the equation are shown in Pedersen & Rasmussen (1990). The angle of strike is given by:

$$\tan(2\theta_s) = 2\frac{\Gamma_{12}(\Gamma_{11} + \Gamma_{22}) + \Gamma_{13}\Gamma_{23}}{\Gamma_{11}^2 - \Gamma_{22}^2 + \Gamma_{13}^2 - \Gamma_{23}^2} \tag{18}$$

The gravity gradiometer data can be treated as a tensor and by analogy to stress tensors; all the stress equations can be applied to the eigenvalues calculated by Equation (14).

Fitzgerald & Hostein (2005, 2006) represented the eigenvalues  $\lambda_1, \lambda_2$  and  $\lambda_3$  analogous to the Mohr diagram, allowing visual reading of the meaning of the eigenvalues of the constitutive relationship from each of the component. This procedure allows checking the quality of data acquisition and/or gravity gradiometer processing. If the Mohr's circle is represented in full, means that the relationship between all components was kept, but if the Mohr's circle is represented in some way incomplete, for example, a straight line segment, means that some component can be compromised. The important issue of this process is that each point of the airborne survey can be represented by a Mohr's circle. Based on this idea this research has implemented a computational routine that calculates the eigenvalues and plotting for each point of the airborne gravity gradiometric survey. Figure 4 shows a computing example for point #5 measurement.

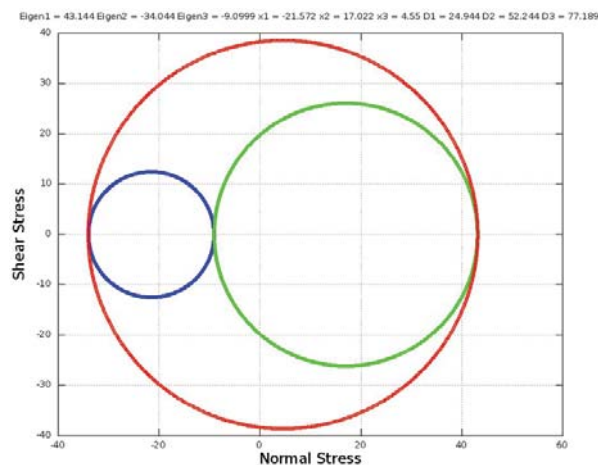


**Figure 4** – Mohr diagram for point #5 measurement. A graph like this was generated for each measurement point of the aerial gravimetric gradiometer survey for checking the quality of the acquisition and/or data processing.

Other techniques used to interpret the tensor data of the gravity or magnetic gradient were presented in Heath (2007), Murphy & Brewster (2007), Beiki et al. (2011), and Toth (2002). Systematically, it is observed that most studies (Murphy, 2007; Mataragio & Kielely, 2009) drew on the relations established by interpreting the torsion balance. For example, the components  $\Gamma_{1,3}$ ,  $\Gamma_{2,3}$ ,  $\Gamma_{1,2}$  and  $\Gamma_{\Delta}$ <sup>9</sup> refer to the elements of the Eötvös tensor measured by torsion balance.  $\Gamma_{1,3}$  and  $\Gamma_{2,3}$  are known as gradient components while  $\Gamma_{1,2}$  and  $\Gamma_{\Delta}$  as curvature components (Toth, 2002).

By covenant the gradient values are represented by vectors and curvatures of the line segment (Toth, 2002). Thus we have the following relationships:

$$\Gamma_{\Delta} = \Gamma_{2,2} - \Gamma_{1,1} \tag{19a}$$

$$\tan \alpha = \frac{\Gamma_{2,3}}{\Gamma_{1,3}} \quad \text{and} \tag{19b}$$

$$\Gamma_{SZ} = \sqrt{\Gamma_{1,3}^2 + \Gamma_{2,3}^2} \tag{19c}$$

These expressions can be used to calculate the azimuth (Eq. 19b) and the magnitude of the gradient vector (Eq. 19c). Another interesting relationship addressed in the papers of Murphy (2007) and Mataragio & Kielely (2009) was named *Invar-TxyTxx-Tyy* and represents the magnitude of the curvature defined as:

$$R = \sqrt{\Gamma_{\Delta}^2 + (2\Gamma_{1,2})^2} \tag{20}$$

Finally, the azimuth of maximum curvature can be represented by:

$$\tan 2\alpha = \frac{-2\Gamma_{1,2}}{\Gamma_{\Delta}} \tag{21}$$

According to the previous information, the azimuth  $\alpha$  and the length  $R$  can be represented on a map as a line segment.

Beiki (2010) proposed to apply the analytic signal technique to the gravity gradient tensor data to estimate source location. Based on the analytical signal of a 2D source potential field, the author applied the Nabighian (1984) approach, using the Hilbert transform while taking advantage of the result of Roest et al. (1992) for the 3D, deduced that the directional analytical signal amplitude for Gravity Gradiometer Tensor (GGT) can be expressed by the following Equations 22(a,b,c):

$$|A_x| = \sqrt{\Gamma_{11}^2 + \Gamma_{12}^2 + \Gamma_{13}^2}, \tag{22a}$$

$$|A_y| = \sqrt{\Gamma_{12}^2 + \Gamma_{22}^2 + \Gamma_{23}^2}, \tag{22b}$$

$$|A_z| = \sqrt{\Gamma_{13}^2 + \Gamma_{23}^2 + \Gamma_{33}^2}. \tag{22c}$$

Another function that tends to locate the maximum over the edges of the anomaly of the source is the amplitude of the Horizontal Gradient (AGH) – (Cordell & Grauch, 1985 *apud* Beiki, 2010). Note that this result is of the same magnitude (Equation 19c).

$$AGH = \sqrt{\Gamma_{1,3}^2 + \Gamma_{2,3}^2} \tag{23}$$

Oruç & Keskinsezer (2008) applied the methodology of the tilt derivative (phase or inclination of the analytical signal) to the GGT data. A phase filter may be defined as a tilt derivative (Miller & Singh, 1994). The tilt derivative is the ratio of the first vertical derivative of the potential field  $f$  and the horizontal gradient amplitude; hence the tilt derivative map can be seen as a normalization of the vertical derivative which is defined as:

$$Tilt = \arctan \left( \frac{\frac{\partial f}{\partial z}}{\sqrt{\left(\frac{\partial f}{\partial x}\right)^2 + \left(\frac{\partial f}{\partial y}\right)^2}} \right) \tag{24}$$

The tilt derivative has an interesting property. As a ratio of dimensionality it responds well to shallow and deep sources and to a broad range of amplitudes for sources at the same level; and being the tangent defined between  $-\pi/2$  and  $\pi/2$ , the application of the tilt derivative allows an easy interpretation of potential field data.

The inclination of the analytical signal can be applied to interpret the gravity gradiometer tensor data yielding the following relationships between the components (Oruç & Keskinseger, 2008):

$$\theta_x = \arctan \left( \frac{\Gamma_{1,3}}{\sqrt{\Gamma_{1,1}^2 + \Gamma_{1,2}^2}} \right) \tag{25}$$

$$\theta_y = \arctan \left( \frac{\Gamma_{2,3}}{\sqrt{\Gamma_{1,2}^2 + \Gamma_{2,2}^2}} \right) \quad \text{and} \tag{26}$$

$$\theta_z = \arctan \left( \frac{\Gamma_{3,3}}{\sqrt{\Gamma_{1,3}^2 + \Gamma_{2,3}^2}} \right) \tag{27}$$

<sup>9</sup>The same as curvature.

Another technique called Experimental combination (EC) has been proposed by Heath (2007), where various combinations of the Magnetic Gradient Tensor (MGT) are possible. This work applied the EC to the GGT airborne data. Some of the products showed interesting results and it is highly recommended to ap-

ply this technique to gravity gradiometer data. Subsequently, each of the possible combinations is going to be presented. To facilitate the understanding related to the coordinate system the components are represented by indices 1 = x, 2 = y and 3 = z.

Equations 28(a) to (o) show all possible combinations of two components.

Equations (28)		
$\Gamma_{xxyy} = \Gamma_{xx} \cdot \Gamma_{yy}$ (a)	$\Gamma_{xxyz} = \Gamma_{xx} \cdot \Gamma_{yz}$ (f)	$\Gamma_{yyxy} = \Gamma_{yy} \cdot \Gamma_{xy}$ (k)
$\Gamma_{xxzz} = \Gamma_{xx} \cdot \Gamma_{zz}$ (b)	$\Gamma_{xxxz} = \Gamma_{xx} \cdot \Gamma_{xz}$ (g)	$\Gamma_{yyyz} = \Gamma_{yy} \cdot \Gamma_{yz}$ (l)
$\Gamma_{xxyy} = \Gamma_{xx} \cdot \Gamma_{xy}$ (c)	$\Gamma_{yyzz} = \Gamma_{yy} \cdot \Gamma_{zz}$ (h)	$\Gamma_{yyxz} = \Gamma_{yy} \cdot \Gamma_{xz}$ (m)
$\Gamma_{xyxz} = \Gamma_{xy} \cdot \Gamma_{xz}$ (d)	$\Gamma_{zzyz} = \Gamma_{zz} \cdot \Gamma_{yz}$ (i)	$\Gamma_{xyyz} = \Gamma_{xy} \cdot \Gamma_{yz}$ (n)
$\Gamma_{yzzz} = \Gamma_{yz} \cdot \Gamma_{xz}$ (e)	$\Gamma_{zzxz} = \Gamma_{zz} \cdot \Gamma_{xz}$ (j)	$\Gamma_{zzxy} = \Gamma_{zz} \cdot \Gamma_{xy}$ (o)

Equations 29(a) to (t) show all possible combinations for three components.

Equations (29)			
$\Gamma_{xxyyzz} = \Gamma_{xx} \cdot \Gamma_{yy} \cdot \Gamma_{zz}$ (a)	$\Gamma_{xxxzxy} = \Gamma_{xx} \cdot \Gamma_{zz} \cdot \Gamma_{xy}$ (f)	$\Gamma_{xxxxyz} = \Gamma_{xx} \cdot \Gamma_{xy} \cdot \Gamma_{xz}$ (k)	$\Gamma_{yyzzxz} = \Gamma_{yy} \cdot \Gamma_{zz} \cdot \Gamma_{xz}$ (p)
$\Gamma_{xxyyxy} = \Gamma_{xx} \cdot \Gamma_{yy} \cdot \Gamma_{xy}$ (b)	$\Gamma_{xxxzyz} = \Gamma_{xx} \cdot \Gamma_{zz} \cdot \Gamma_{yz}$ (g)	$\Gamma_{xxyzxx} = \Gamma_{xx} \cdot \Gamma_{yz} \cdot \Gamma_{xz}$ (l)	$\Gamma_{yyxyyz} = \Gamma_{yy} \cdot \Gamma_{xy} \cdot \Gamma_{yz}$ (q)
$\Gamma_{xxyyyz} = \Gamma_{xx} \cdot \Gamma_{yy} \cdot \Gamma_{yz}$ (c)	$\Gamma_{xxxzxx} = \Gamma_{xx} \cdot \Gamma_{zz} \cdot \Gamma_{xz}$ (h)	$\Gamma_{yyzzxy} = \Gamma_{yy} \cdot \Gamma_{zz} \cdot \Gamma_{xy}$ (m)	$\Gamma_{yyxyxz} = \Gamma_{yy} \cdot \Gamma_{xy} \cdot \Gamma_{xz}$ (r)
$\Gamma_{xxyyxx} = \Gamma_{xx} \cdot \Gamma_{yy} \cdot \Gamma_{xz}$ (d)	$\Gamma_{xxxxyz} = \Gamma_{xx} \cdot \Gamma_{xy} \cdot \Gamma_{yz}$ (i)	$\Gamma_{yyzzyz} = \Gamma_{yy} \cdot \Gamma_{zz} \cdot \Gamma_{yz}$ (n)	$\Gamma_{yyyzxz} = \Gamma_{yy} \cdot \Gamma_{yz} \cdot \Gamma_{xz}$ (s)
$\Gamma_{zzxyyz} = \Gamma_{zz} \cdot \Gamma_{xy} \cdot \Gamma_{yz}$ (e)	$\Gamma_{zzxyxz} = \Gamma_{zz} \cdot \Gamma_{xy} \cdot \Gamma_{xz}$ (j)	$\Gamma_{zzyzxz} = \Gamma_{zz} \cdot \Gamma_{yz} \cdot \Gamma_{xz}$ (o)	$\Gamma_{xyyzxz} = \Gamma_{xy} \cdot \Gamma_{yz} \cdot \Gamma_{xz}$ (t)

Equations 30(a) to (o) shows all possible combinations for four components.

Equations (30)		
$\Gamma_{xxyyzzxy} = \Gamma_{xx} \cdot \Gamma_{yy} \cdot \Gamma_{zz} \cdot \Gamma_{xy}$ (a)	$\Gamma_{xxyyzzxz} = \Gamma_{xx} \cdot \Gamma_{yy} \cdot \Gamma_{zz} \cdot \Gamma_{xz}$ (f)	$\Gamma_{yyzzxyyz} = \Gamma_{yy} \cdot \Gamma_{zz} \cdot \Gamma_{xy} \cdot \Gamma_{yz}$ (k)
$\Gamma_{xxyyzzyz} = \Gamma_{xx} \cdot \Gamma_{yy} \cdot \Gamma_{zz} \cdot \Gamma_{yz}$ (b)	$\Gamma_{xxxzxyyz} = \Gamma_{xx} \cdot \Gamma_{zz} \cdot \Gamma_{xy} \cdot \Gamma_{yz}$ (g)	$\Gamma_{yyzzxyxz} = \Gamma_{yy} \cdot \Gamma_{zz} \cdot \Gamma_{xy} \cdot \Gamma_{xz}$ (l)
$\Gamma_{xxyyzzxz} = \Gamma_{xx} \cdot \Gamma_{yy} \cdot \Gamma_{zz} \cdot \Gamma_{xz}$ (c)	$\Gamma_{xxxzxyxz} = \Gamma_{xx} \cdot \Gamma_{zz} \cdot \Gamma_{xy} \cdot \Gamma_{xz}$ (h)	$\Gamma_{yyzzyzxz} = \Gamma_{yy} \cdot \Gamma_{zz} \cdot \Gamma_{yz} \cdot \Gamma_{xz}$ (m)
$\Gamma_{xxyyxyyz} = \Gamma_{xx} \cdot \Gamma_{yy} \cdot \Gamma_{xy} \cdot \Gamma_{yz}$ (d)	$\Gamma_{xxxzyzxx} = \Gamma_{xx} \cdot \Gamma_{zz} \cdot \Gamma_{yz} \cdot \Gamma_{xz}$ (i)	$\Gamma_{yyxyyzxz} = \Gamma_{yy} \cdot \Gamma_{xy} \cdot \Gamma_{yz} \cdot \Gamma_{xz}$ (n)
$\Gamma_{xxyyxyxz} = \Gamma_{xx} \cdot \Gamma_{yy} \cdot \Gamma_{xy} \cdot \Gamma_{xz}$ (e)	$\Gamma_{xxxzyzxx} = \Gamma_{xx} \cdot \Gamma_{xy} \cdot \Gamma_{yz} \cdot \Gamma_{xz}$ (j)	$\Gamma_{xxyyzzxz} = \Gamma_{xx} \cdot \Gamma_{yy} \cdot \Gamma_{zz} \cdot \Gamma_{xz}$ (o)

Equations 31(a) to (f) show all possible combinations for five components.

Equations (31)	
$\Gamma_{xxyyzzxyyz} = \Gamma_{xx} \cdot \Gamma_{yy} \cdot \Gamma_{zz} \cdot \Gamma_{xy} \cdot \Gamma_{yz}$ (a)	$\Gamma_{xxyyxyyzxz} = \Gamma_{xx} \cdot \Gamma_{yy} \cdot \Gamma_{xy} \cdot \Gamma_{yz} \cdot \Gamma_{xz}$ (d)
$\Gamma_{xxyyzzxyxz} = \Gamma_{xx} \cdot \Gamma_{yy} \cdot \Gamma_{zz} \cdot \Gamma_{xy} \cdot \Gamma_{xz}$ (b)	$\Gamma_{xxxzxyyzxz} = \Gamma_{xx} \cdot \Gamma_{yy} \cdot \Gamma_{xy} \cdot \Gamma_{yz} \cdot \Gamma_{xz}$ (e)
$\Gamma_{xxyyzzyzxz} = \Gamma_{xx} \cdot \Gamma_{yy} \cdot \Gamma_{zz} \cdot \Gamma_{yz} \cdot \Gamma_{xz}$ (c)	$\Gamma_{yyzzxyyzxz} = \Gamma_{yy} \cdot \Gamma_{zz} \cdot \Gamma_{xy} \cdot \Gamma_{yz} \cdot \Gamma_{xz}$ (f)

Finally equation (32) shows all possible combinations for six the components of the gravity gradient tensor.

$$\Gamma_{xxyyzzxyyzxz} = \Gamma_{xx} \cdot \Gamma_{yy} \cdot \Gamma_{zz} \cdot \Gamma_{xy} \cdot \Gamma_{yz} \cdot \Gamma_{xz} \tag{32}$$

Heath (2007) developed a modified determinant (Eq. 33). Starting from the calculation of the determinant equation:

$$\Gamma_{\det} = \begin{vmatrix} \bar{\Gamma}_{1,1} & \bar{\Gamma}_{1,2} & \bar{\Gamma}_{1,3} \\ \bar{\Gamma}_{2,1} & \bar{\Gamma}_{2,2} & \bar{\Gamma}_{2,3} \\ \bar{\Gamma}_{3,1} & \bar{\Gamma}_{3,2} & \bar{\Gamma}_{3,3} \end{vmatrix} = \bar{\Gamma}_{1,1} \cdot \bar{\Gamma}_{2,2} \cdot \bar{\Gamma}_{3,3} + 2 \cdot \bar{\Gamma}_{1,2} \cdot \bar{\Gamma}_{2,3} \cdot \bar{\Gamma}_{1,3} - \bar{\Gamma}_{2,3}^2 \cdot \bar{\Gamma}_{1,1} - \bar{\Gamma}_{1,3}^2 \cdot \bar{\Gamma}_{2,2} - \bar{\Gamma}_{1,2}^2 \cdot \bar{\Gamma}_{3,3} \tag{33}$$

one comes easily to the equation (34)

$$\Gamma_{\det_{\text{mod}}} = \sqrt{(\Gamma_{1,1} \cdot \Gamma_{2,2} \cdot \Gamma_{3,3})^2 + (2 \cdot \Gamma_{1,2} \cdot \Gamma_{2,3} \cdot \Gamma_{1,3})^2 + (\Gamma_{2,3}^2 \cdot \Gamma_{1,1})^2 + (\Gamma_{1,3}^2 \cdot \Gamma_{2,2})^2 + (\Gamma_{1,2}^2 \cdot \Gamma_{3,3})^2} \tag{34}$$

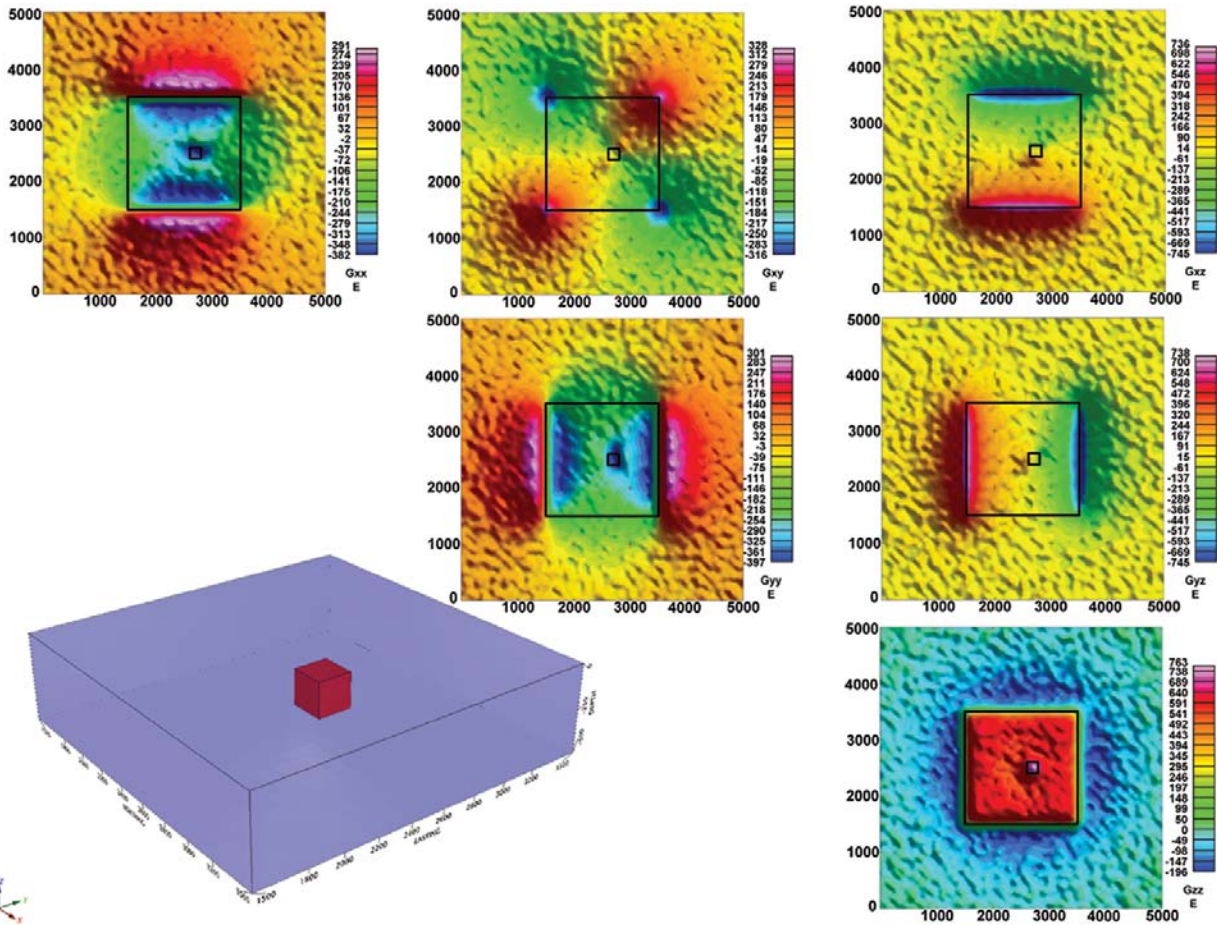


**Figure 5** – 3D model representing the compact itabirite (blue) of the host rock and the block of hematite (red) inscribed in the host rock. In that order from left to right are shown the components  $G_{xx}(\Gamma_{1,1})$ ,  $G_{xy}(\Gamma_{1,2})$ ,  $G_{xz}(\Gamma_{1,3})$ ,  $G_{yy}(\Gamma_{2,2})$ ,  $G_{yz}(\Gamma_{2,3})$  and  $G_{zz}(\Gamma_{3,3})$ .

**SYNTHETIC DATA**

The synthetic model (Nagy et al., 2000, 2001), built for application of codes developed for processing and interpretation of airborne gravity gradiometer was generated starting with a similar example situated in the airborne gravity gradiometer survey named Boa 6, in the Quadrilátero Ferrífero of Minas Gerais State (Carlos et al., 2011).

A cube with dimensions of 200 m × 200 m × 200 m, with its top at a depth of approximately 50 m below ground level was generated; this cube may represent compact hematite, for example. The average density of the compact hematite is of 4200 kg/m<sup>3</sup>. Another polygon, with dimensions 2000 m × 2000 m × 500 m, was generated representing compact itabirite, the host rock, with an average density of 3200 kg/m<sup>3</sup>.

Figure 5 shows the synthetic model designed to simulate the signal of hematite in the host rock of compact itabirite. The den-

sity contrast of the mineral of interest related to the host is of 1000 kg/m<sup>3</sup>. The blue polygon is the host rock or compact itabirite while the red polygon represents hematite with top 50 m below the surface.

Upon observing Figure 5 only those components that can be interpreted directly, using the response of the gravity gradiometry components are  $G_{zz}$ ,  $G_{xz}$  and  $G_{yz}$ , representing the geology of surface/subsurface, the center of mass in the east-west and the center of mass in the north south direction, respectively. Some authors (Braga et al., 2010; Mataragio et al., 2011) interpret the  $G_{xx}$ ,  $G_{xy}$  and  $G_{yy}$  components such as: “mapping the northern and southern edges of the source; mapping the corners of the source; and mapping the eastern and western edges”, respectively. These last three components are not valid for deeper sources; therefore, the idea that these features are mapped by the last three components is not completely valid.

The results shown in Figure 6 are related to equations (10), (11) and (12). The invariants are 0, 1 and 2 ( $I_0$ ,  $I_1$  and  $I_2$ ). Notice that the sum of the main diagonal, or trace of the tensor ( $I_0$ ), is a network of residual without geological significance for interpretation, but expresses the quality of maintenance of the relationship between the components of the gravity gradiometry tensor.  $I_1$  can be related to both tensor components and the eigenvalues. Note that mapping edges (negative values) of the host rock (itabirite) and the hematite contained in the itabirite

is very clear.  $I_2$ , as  $I_1$ , is related to both components and/or eigenvalues. Also note that  $I_2$ , the tensor determinant, and  $I_1$  have opposite patterns so these two products must always be interpreted together.

Eigenvalues 1, 2 and 3 were calculated using equations (14). Note that the patterns related to  $\lambda_1$  and  $\lambda_2$  are easier to analyze. Possibly,  $\lambda_3$  maps the corners of both the host rock and the hematite (Fig. 7).

The following processing, based on Tóth (2002) is the focus

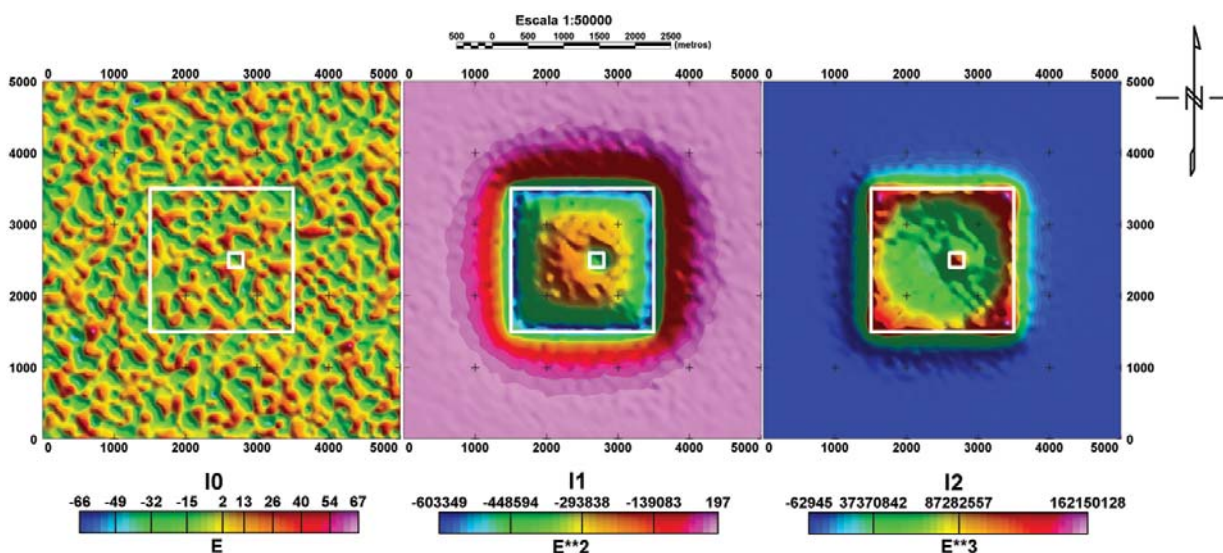


Figure 6 – Invariant 0, 1 and 2. The large white polygon shows the host rock while the small inscribed polygon shows the rock of interest.

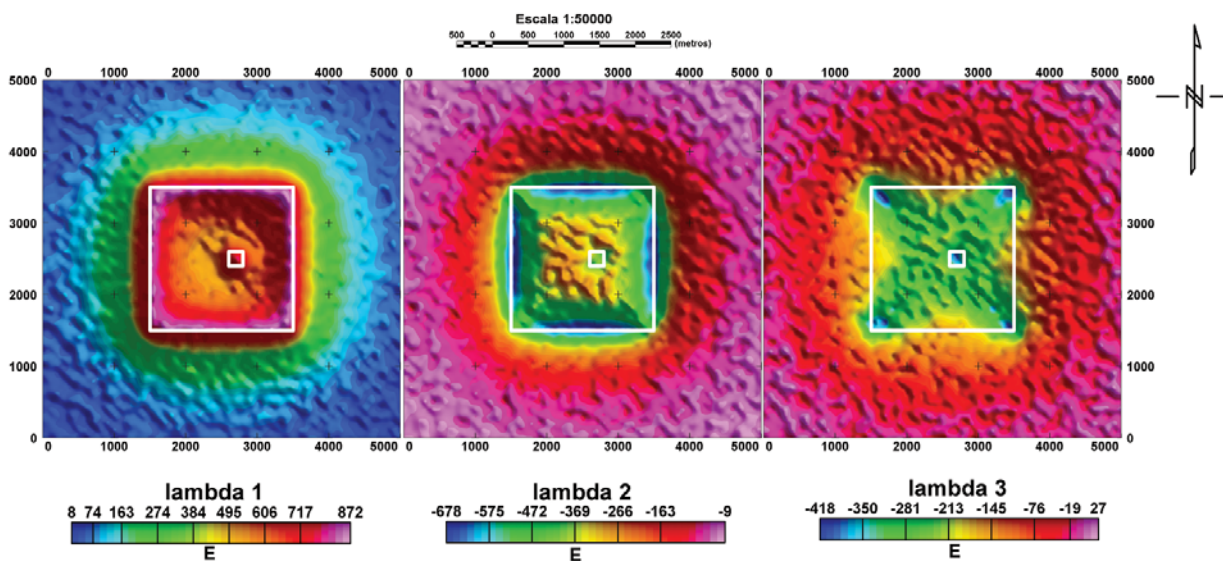


Figure 7 – Eigenvalues 1, 2 and 3. The large polygon shows hematite while the smaller shows the host/enclosing rocks, for example, itabirite.

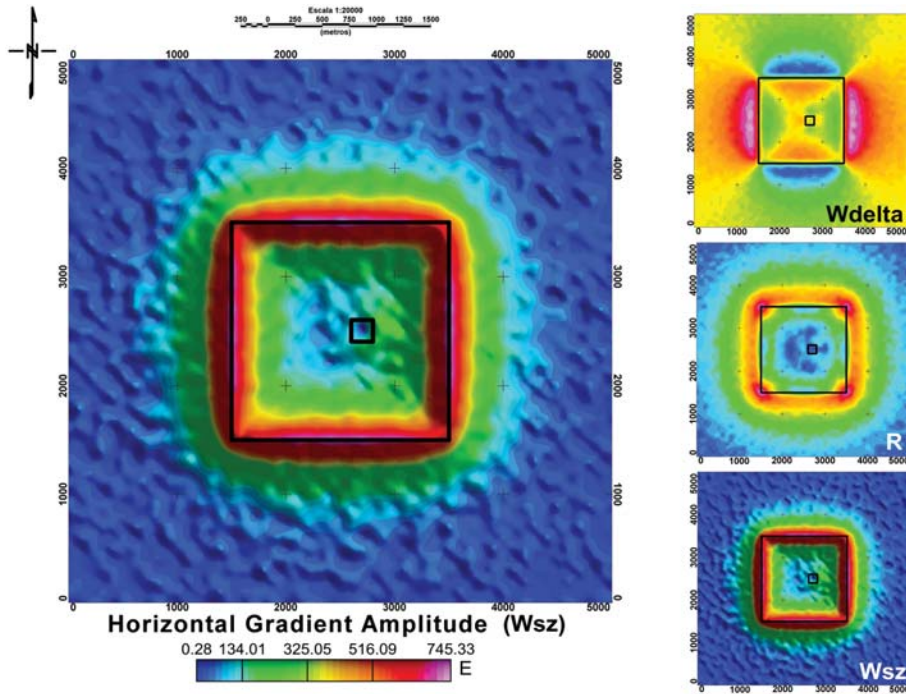


Figure 8 –  $W_{Delta}$  (curvature),  $R$  (magnitude of curvature) and  $W_{sz}$  (amplitude of the horizontal gradient) based on Tóth (2002).

of the Hungarian school with roots in the torsion balance, which was the forerunner of modern systems of gravity gradiometry. The nomenclatures used in Figure 8 are:  $W_{delta}$  (curvature<sup>10</sup>), related to the first Equation (19a),  $R$  (magnitude of curvature), Equation (20) and finally  $W_{sz}$  (gradient magnitude in the  $z$  direction), Equation (19c).

Figure 8 shows that the gradient magnitude mapped accurately the boundaries of the host rock and the fact that a high value of density contrast occurs beyond this limit. The hematite contained in the itabirite is mapped as low magnitude gradient value. Normally the curvature ( $W_{delta}$ ) in real data is difficult to interpret, but in this case the boundaries were mapped as positive anomalies in the east-west direction and negative in north-south. Finally, the magnitude of curvature ( $R$ ) accurately mapped the corners of the host rock, probably because this rock is outcropping.

Figure 9 shows the result of the processing carried out by Beiki & Pedersen (2010). It can be observed that the amplitude of the directional analytic signal in the  $z$  direction maps the host rock as well as hematite. Moreover, the analytical signal in the  $x$  and  $y$  directions maps the boundaries of the host rock in the north-south and east-west directions, respectively. Hematite, de-

spite the relatively weak signal, was mapped in the three amplitudes of the directional analytic signal.

Figure 10 shows the result of the methodology of processing developed by Oruç & Keskinsezer (2008). Note that the theta  $z(\theta_z)$  mapped with excellent resolution the limits of the host rock while the hematite is not visible.  $Theta x(\theta_x)$  and  $theta y(\theta_y)$  mapped, respectively, the north-south and east-west boundaries of the host rock.

The experimental combinations<sup>11</sup> of the two components of the gravity gradient tensor are shown in Figure 11. It is noteworthy that the combinations offer many possibilities of interpretation such as:  $xyy$ ,  $xxzz$ ,  $xxxz$  and  $yyzz$ , mapping the host rock and the hematite in each of these combinations, as well as other possibilities such as the limits ( $xyyz$ ,  $zzyz$ ,  $zzxz$ ,  $yyyz$  and  $yyxz$ ) or even the corners ( $xyxz$ ,  $yzxz$ ,  $xyyz$  and  $xxxy$ ) of the host rock.

The combination of three components (Fig. 12) can map the host rock and the hematite ( $xyyzz$ ), the limits of the host rock ( $xyyyz$ ,  $xyyxxz$ ,  $xxzzyz$ ,  $xxzzxz$ ,  $yyzzyz$  and  $yyzzxz$ ) and even the corners of the host rock ( $xyyxy$ ,  $zzyyyz$ ,  $xxzzyx$ ,  $xxxyyz$ ,  $zzxyxz$  and  $xyyxxz$ , for example).

<sup>10</sup>The curvature is represented only by the subtraction of the  $G_{yy}$  and  $G_{xx}$  components. The curvatures of the Falcon and 3D-FTG systems are multiplied by 1/2, that is,  $\Gamma_{\Delta} = \frac{\Gamma_{2,2} - \Gamma_{1,1}}{2}$ .

<sup>11</sup>Literally, it means a simple combinatorial, that is, there is no repetition of any element in each group of  $p$  elements. In canonical form, we have:  $C_{m,p} = \frac{m!}{(m-p)!p!}$ .

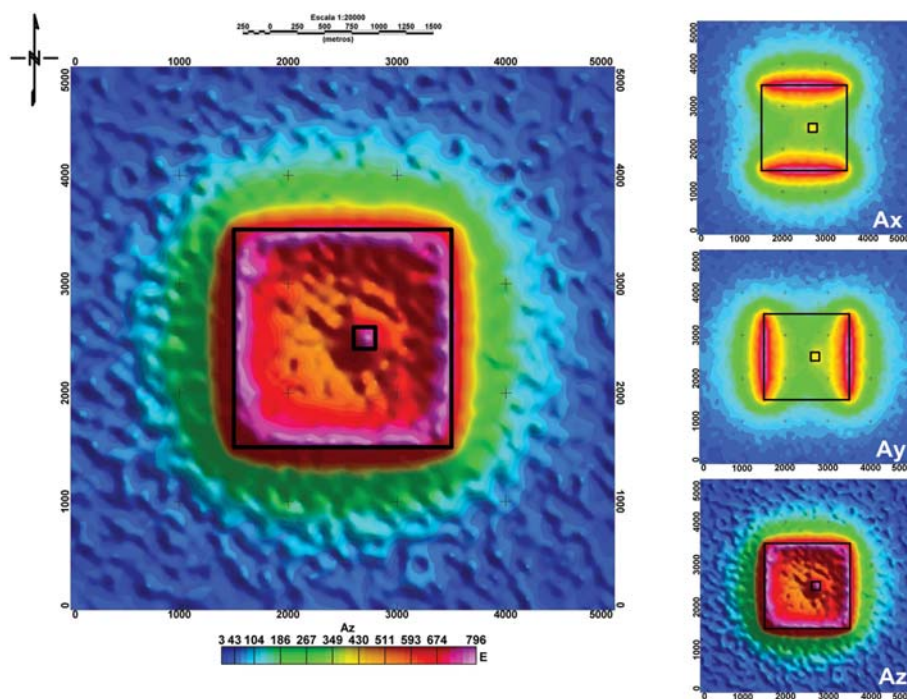


Figure 9 – Calculation of the directional analytic signal in the  $x$ ,  $y$  and  $z$  directions ( $A_x$ ,  $A_y$  and  $A_z$ , respectively).

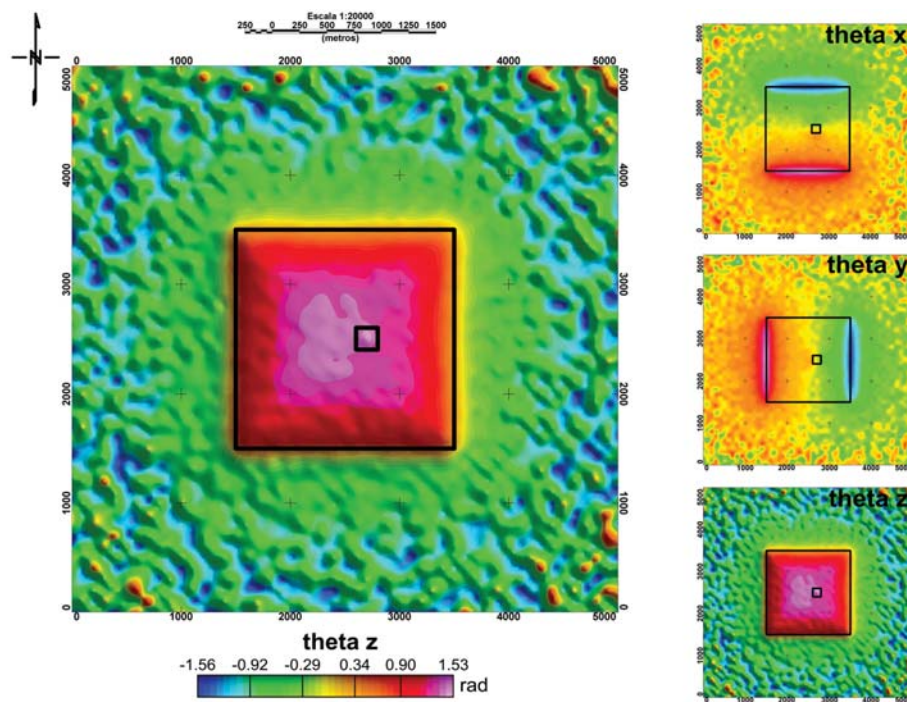


Figure 10 –  $\theta_x$ ,  $\theta_y$  and  $\theta_z$  according to Oruç & Keskinsezer (2008).

The combination of four components of the gravity gradiometer tensor shows that the standards of representation of the feature limits become scarcer as seen in Figure 13. Only the combina-

tions  $xyyzzyz$  and  $xyyzzxz$  were able to provide this information. All other combinations of four components showed a pattern of delimitation of the corners of the host rock.

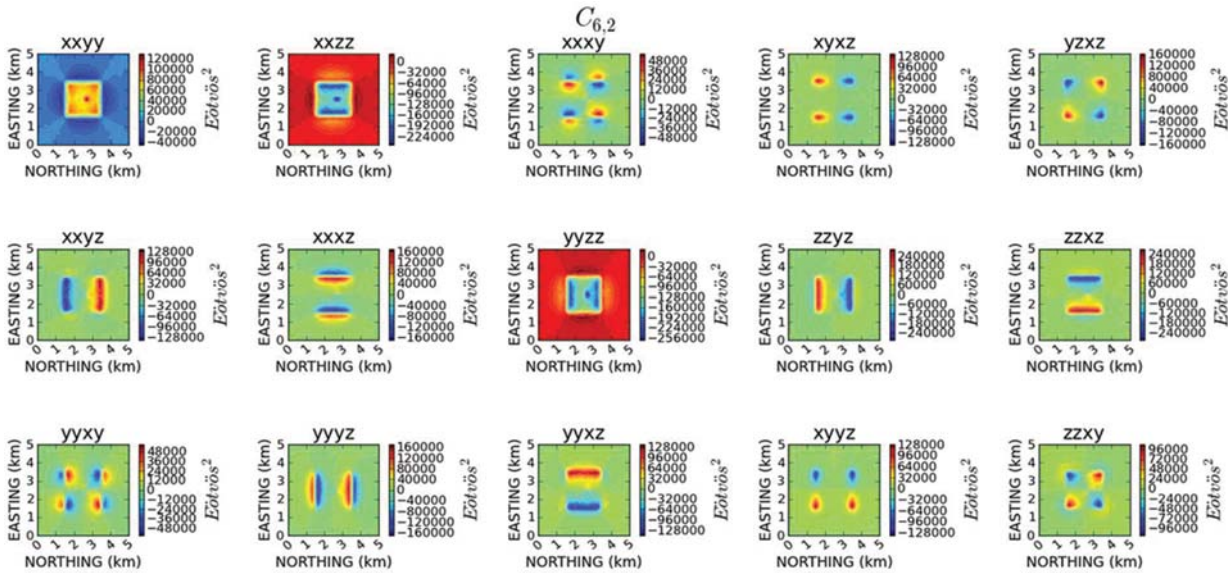


Figure 11 – Combination of two components ( $C_{6,2}$ ).

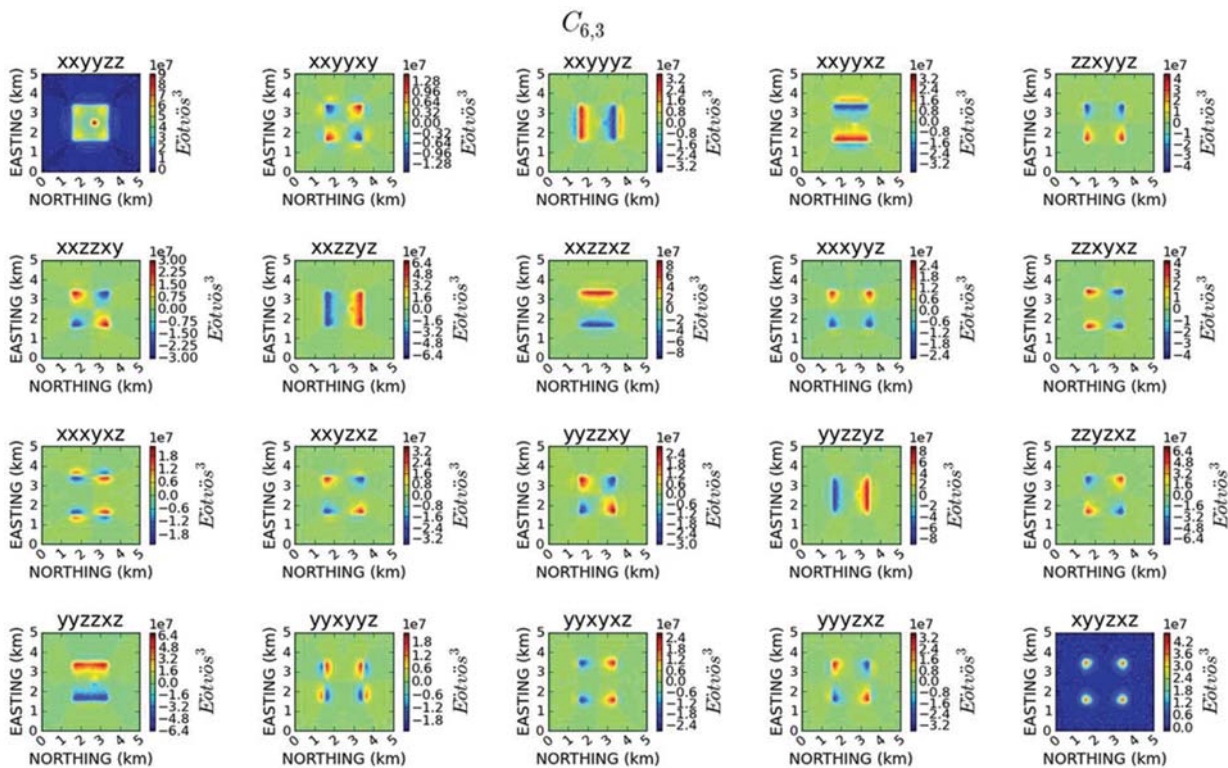


Figure 12 – Combination of three components ( $C_{6,3}$ ).

Figure 14 shows the combination of five components ( $C_{6,5}$ ) while the lower left corner of the same Figure shows the combination of six components ( $C_{6,6}$ ). In general, it can be stated that the pattern represented by the combinations of five and six components represents the corners of the host rocks.

Figure 15 shows the analysis of the two processes proposed by Heath (2007). The first figure to the left shows the Determinant processing, or using the nomenclature of Pederesen and Rasmussen (1990), Invariant 2 or ( $I_2$ ). The figure in the center refers to the modified determinant. Observe that Equation 34

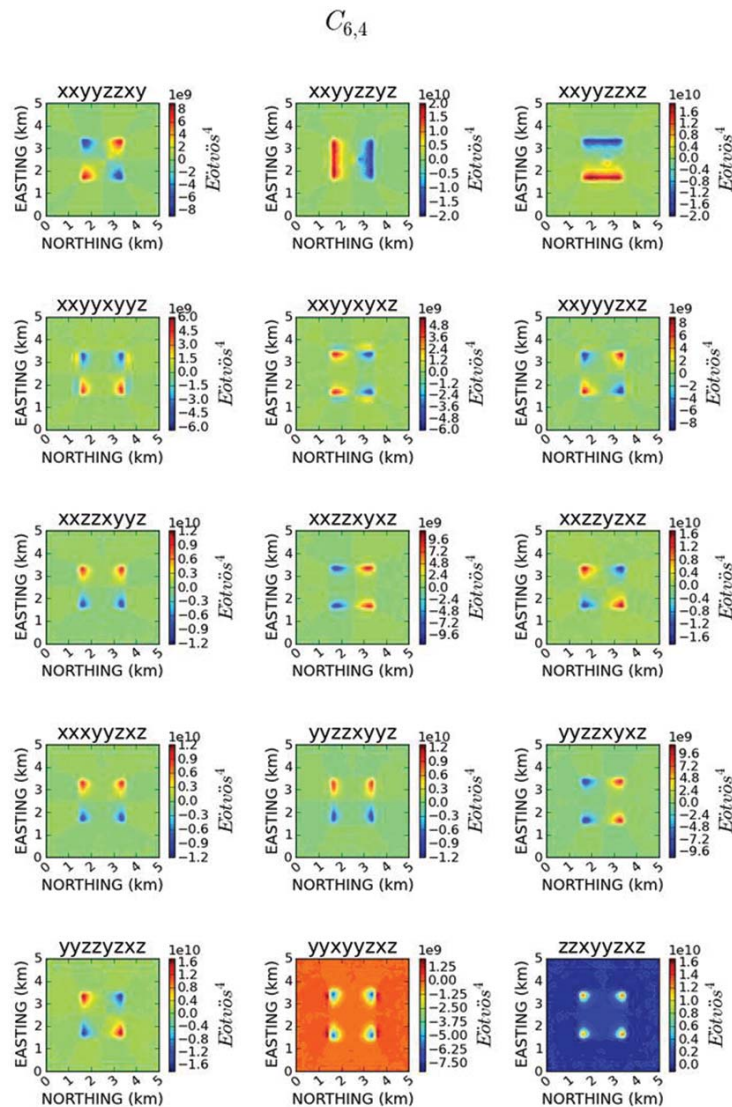


Figure 13 – Combination of four components ( $C_{6,4}$ ).

maps with higher accuracy the boundaries of the host rock because the square root solution restricts the solutions to positive values. This analysis is represented by two profiles placed on the right side of Figure 15. The first profile (L1) cutting only hematite, superimposed on the  $I_2$  shows that the modified determinant defines with higher accuracy the boundaries of the host rock. The same analysis was applied to the second profile (L2), the figure on the lower right corner superimposed on the modified determinant shows that this profile cuts both hematite and host rock. Therefore, it presents the same pattern as before, that is, the modified determinant tends to delineate more accurately the position of the source generating the gravity gradiometer tensor signal.

**REAL DATA**

In this section the same processes are applied to the real data collected in area located in th Quadrilátero Ferrífero, Minas Gerais State. More detailed geology of the area is presented in Braga (2009), Braga et al. (2010) and Carlos et al. (2011).

Figure 16 shows the data without terrain correction. A direct correlation is observed between the features observed in the component  $T_{zz}(G_{zz})$  and the topography of the area. In order to process the gravimetric gradiometer data, the terrain influence must be removed while taking into consideration only the effect of the masses generating signal in the gravity gradiometer. The processing steps are applied to the components corrected for terrain influence.

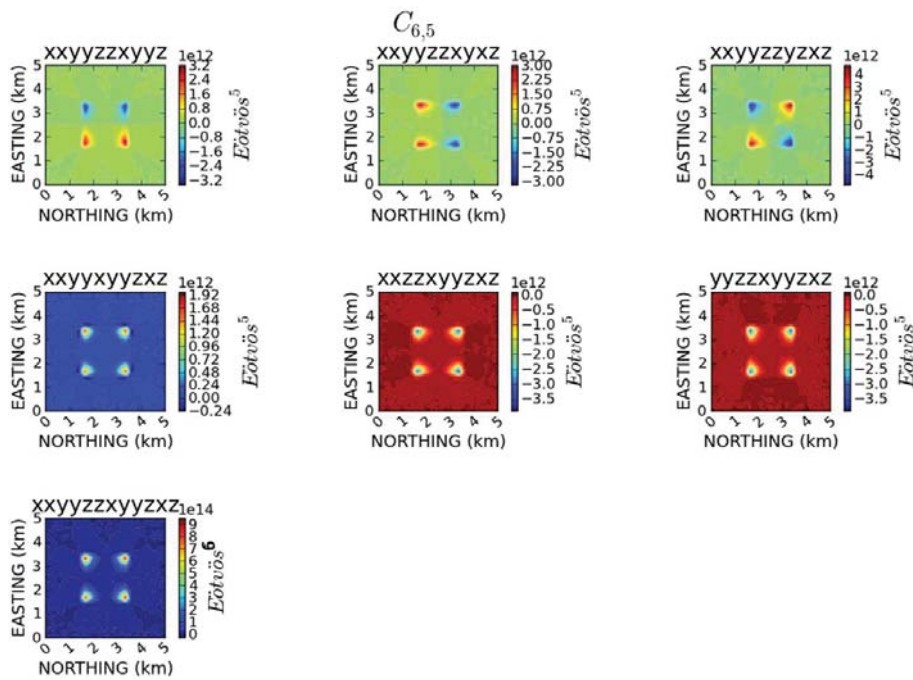


Figure 14 – Combination of five components ( $C_{6,5}$ ). The lower left corner of the last figure shows the combination of all components of the gravimetric gradiometer tensor ( $C_{6,6}$ ).

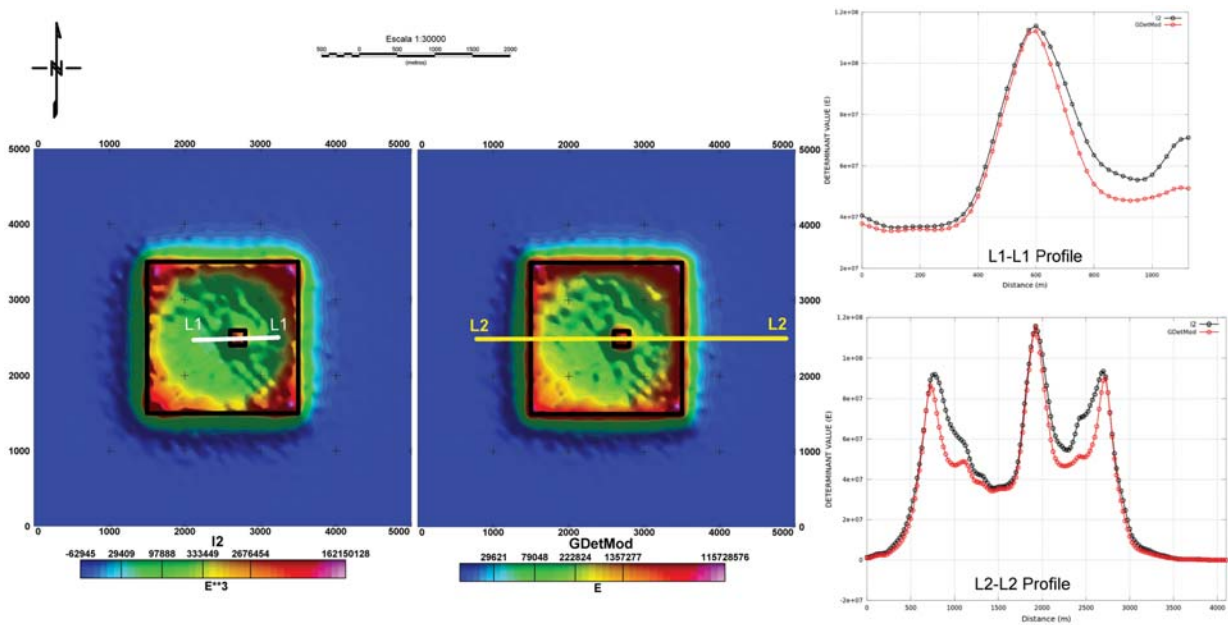


Figure 15 – Invariant 2 ( $\Gamma_{det}$ ), figure on the right and Modified Determinant ( $\Gamma_{detmod}$ ). On the right top panel, the profile is traced over hematite of  $I_2$  (black line) and of the Modified Determinant (red line). The  $\Gamma_{detmod}$  tends to delineate more accurately the position of the anomaly source, profile L1. The same behavior was observed in the lower panel, profile L2, where the black line refers to  $I_2$  and the red line to the modified determinant. The boundaries of the host rock and even the hematite were mapped in greater detail.

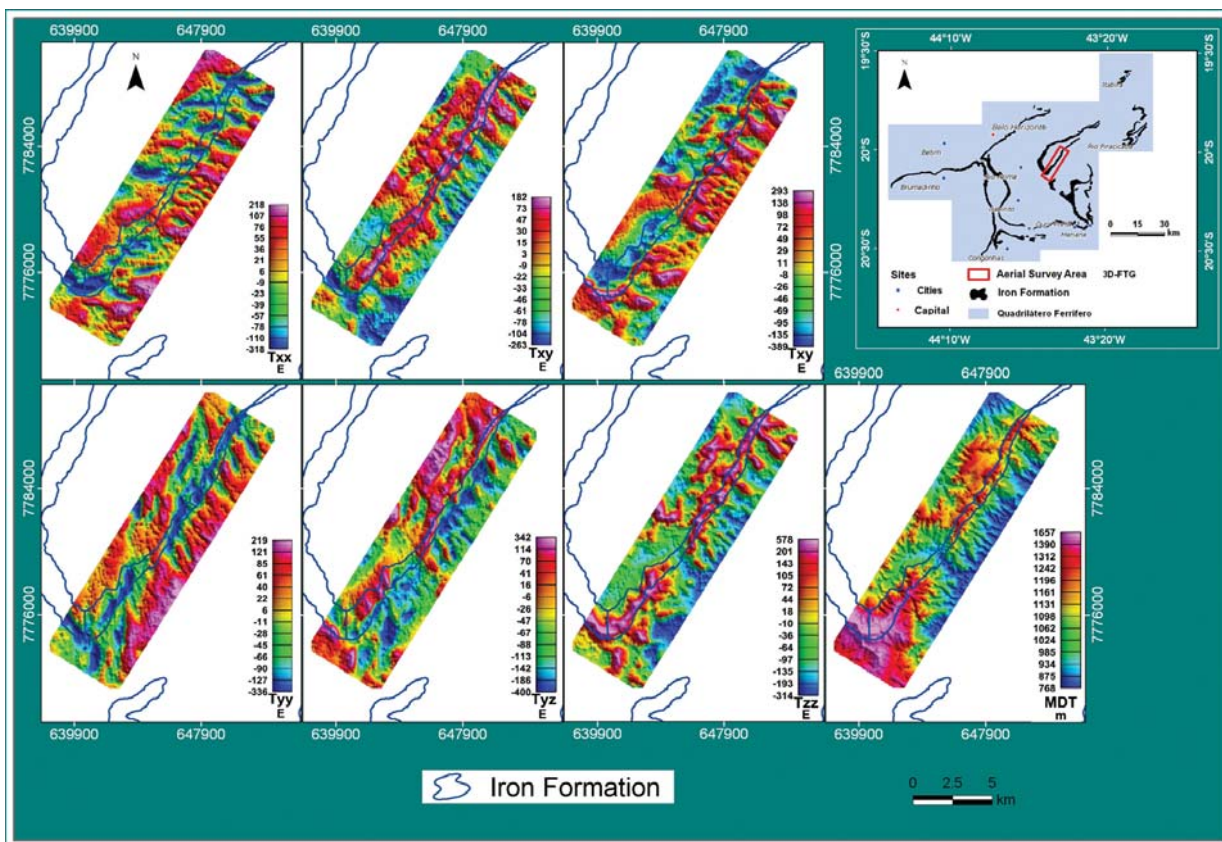


Figure 16 – Components of the airborne gravity gradiometer survey in Boa 6 region. The continuous blue line is the boundary of the iron formation.

Figure 17 shows the data already corrected to the density value of  $2.36 \text{ g/cm}^3$  (Carlos et al., 2011).

It is observed that the signal of the iron formation was mapped accurately by the  $T_{zz}$  component while other components, like  $T_{yy}$  and  $T_{yz}$ , mapped the same feature, with  $T_{yy}$  highlighting the iron formation with negative values and  $T_{yz}$  mapping exactly the boundaries of the iron formation as a positive anomaly to west and negative to east.

Figure 18 shows the processing that uses the invariant and eigenvalues as described in Pedersen & Rasmussen (1990). The invariant  $I_0$  or trace of the tensor presents almost entirely noise and, as expected by the Laplace equation, in which the sum of the components in-line is close to zero this is used for quality control of the acquired data. The pattern of  $I_1$  is the opposite of  $I_2$ , i.e. while the first maps the iron formation with negative signal the second assigns positive values. Interesting results can be observed in the eigenvalues 1, 2 and 3 ( $\lambda_1$ ,  $\lambda_2$  and  $\lambda_3$ ). Notice that  $\lambda_1$  mapped positive values in iron formation, but not all iron formation presents positive values, inclusive

because the breaking of the narrowing of iron formation was observed in field inspections. Eigenvalue 2 presents a negative pattern similar to  $I_1$ . The result of  $\lambda_3$  is the most complex to interpret, with agreement between  $\lambda_1$  and  $\lambda_3$ , though with negative values of the latter.

Figure 19 shows the processing results using the methodology described by Toth (2002). For comparison purposes, the results of synthetic and real data were placed side by side. The amplitude of curvature defines precisely (synthetic model) the corners of the host rock. On the other hand, the processing of the real data was delineated somewhat accurately only the east-west boundary due to the fact that the iron formation geometry is approximately a rectangle that does not close toward north-south. At the curvature, the interpretation is not made separately. It is noted, however, that the east-west boundaries positive anomalies are in agreement with the synthetic model. The result of easy interpretation is the amplitude of the horizontal gradients that define the limits of the iron formation. Note that the east-west boundaries were mapped accurately by the latter process.

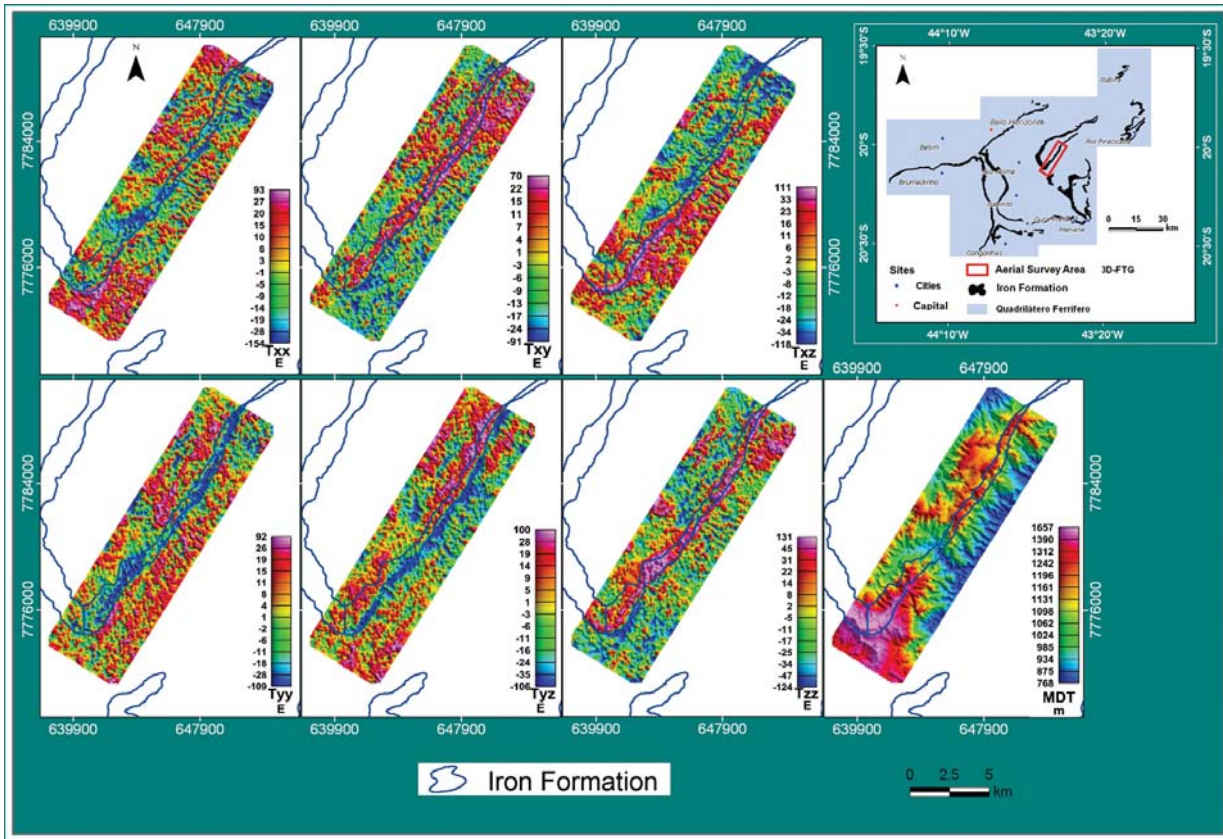


**Figure 17** – Components of the gravity gradiometer tensor corrected to the value of  $2.36 \text{ g/cm}^3$ . The component  $T_{zz}$  no longer presents the same features of the regional topography. The resulting signal\* is only due to the iron formation (continuous blue line) mapped by this component.

\*Unlike the conventional gravimetric method where the influence of deep sources must be removed by applying filters to the residual-regional separation, in gravity gradiometry filters are not always applied for this purpose since the targets of interest for prospecting ore are in the range of several hundred meters (less than 300 meters deep). When host rocks have similar density values of the lithologies of interest (itabirite, hematite, for example) the filter is used to isolate the signal resulting from the lithology and/or desired rocks.

Figure 20 summarizes the results of data processing according to Beiki (2010). The figures in the left panel are: (A) amplitude of the analytic signal in the  $x - (A_x)$  direction, (B) amplitude of the analytic signal in the  $y - (A_y)$  direction, (C) amplitude of the analytic signal in the  $z - (A_z)$  direction and (D) Total Horizontal Gradient (THG or HGA). The result of  $A_x$  is not easy to interpret; however, the others are.  $A_y$  mapped the limits of the iron formation,  $A_z$  mapped beyond the limits, the anomalies of interests inside the iron formation while HGA has already been interpreted in Figure 19.

Figure 21 shows the processing results using the tilt derivative methodology or phase of the analytic signal. The interesting result is  $\theta_y$  that mapped the east-west boundaries showing a positive and a negative anomaly in the west and east regions, respectively, the same pattern of the synthetic model.

The  $\theta_z$  shows virtually the mapping of the iron formation, as in the synthetic model. The  $\theta_x$  cannot be compared to the synthetic model due to the direction of the structures in this area; however, the narrowing of the iron formation in the center of the area indicated accurately the position of a fault mapped in the field.

Figure 22 shows, two by two a simple combination of the six components of the gravity gradiometer tensor. Among the interesting results, the combinations  $xyxy$ ,  $xxzz$  display opposite patterns, such as the analysis with the invariants 1 and 2, but are limited to regions of higher gradients. Patterns that are nearly consistent, as in  $xxzz$  and  $xxxz$  and in  $xyxy$  and  $xyxz$ , and other patterns that virtually map the geometry of the iron formation such as:  $yzxz$ ,  $zzxz$ ,  $yyyyz$ ,  $xyyz$  and  $zzxy$ .

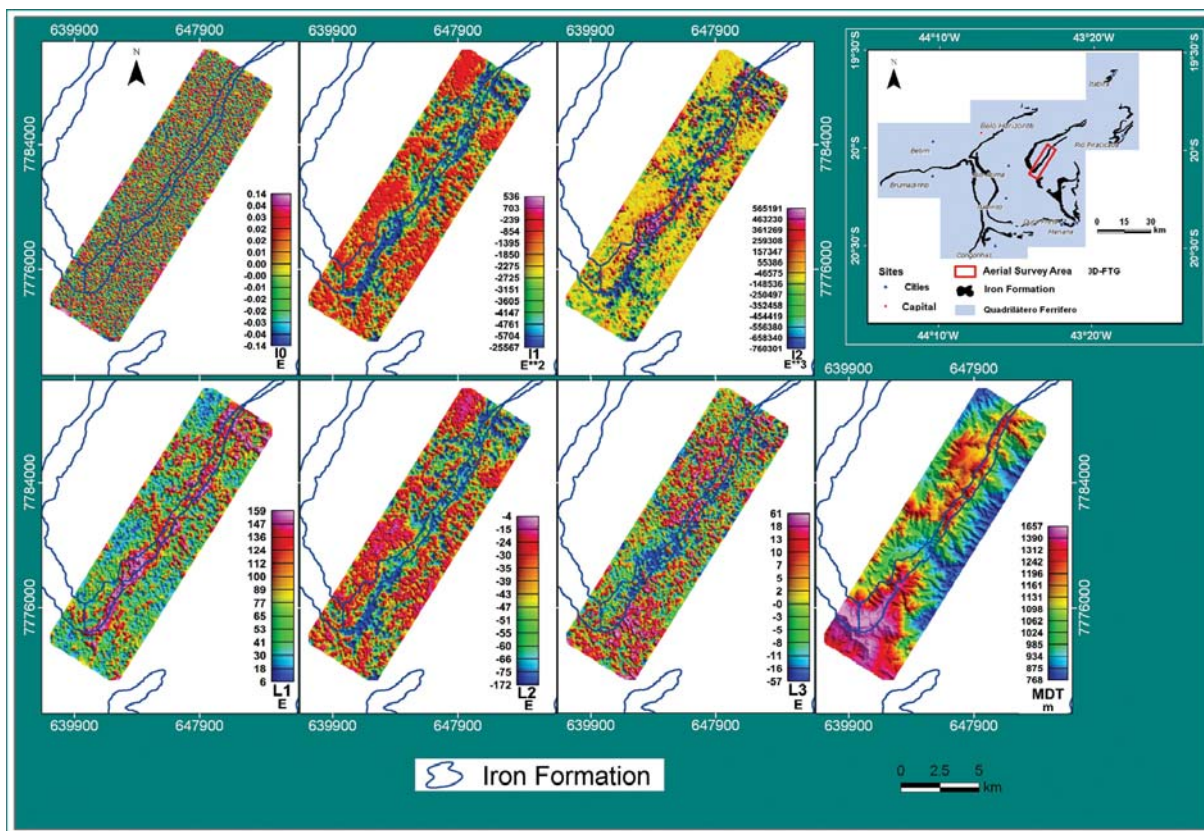


Figure 18 – The upper panel shows the Invariants 0, 1 and 2. The lower panel shows the eigenvalues 1, 2 and 3. The continuous blue line represents the boundaries of the iron formation.

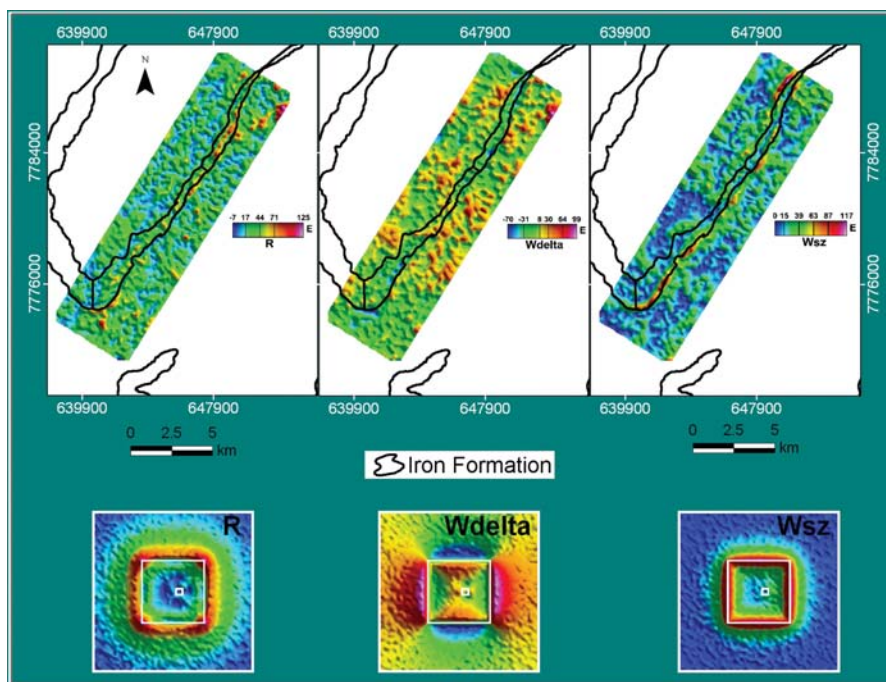
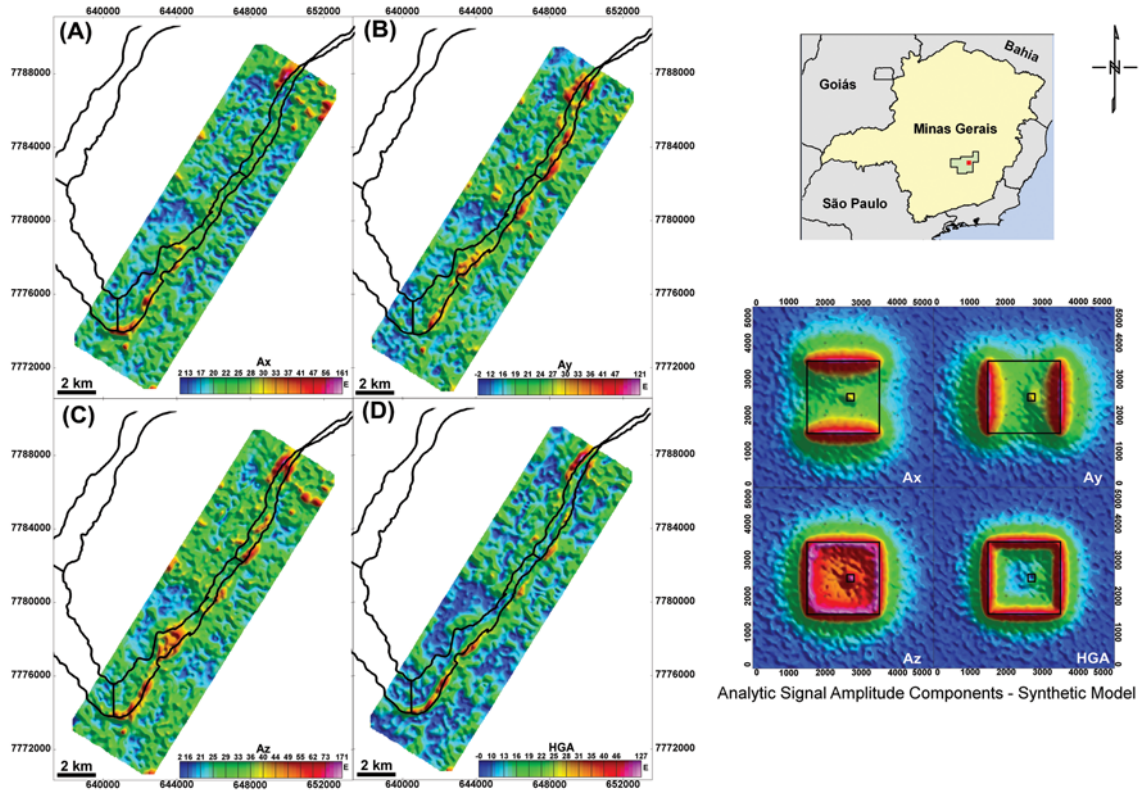
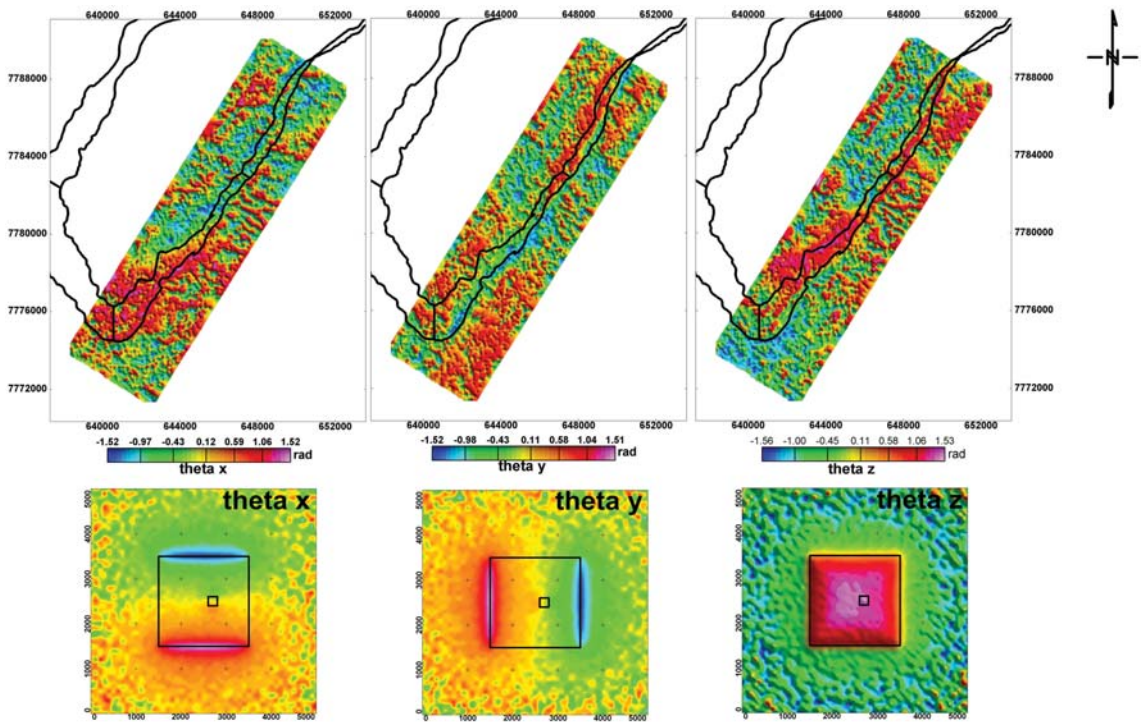


Figure 19 – Curvature amplitude ( $R$ ), Curvature ( $W_{delta}$ ) and Horizontal Gradient amplitude ( $W_{sz}$  or HGA) resulting from the processing of the Boa 6 area. The continuous black line superimposed to the real data represents the boundaries of the iron formation.



**Figure 20** – (A) Amplitude of analytic signal in the  $x$  direction. (B) Amplitude of the analytic signal in the  $y$  direction. (C) Amplitude of analytic signal in the  $z$  direction. (D) Horizontal Gradient Amplitude. The solid black line superimposed on the real data represents the iron formation.



**Figure 21** – Results of the inclination of the analytical signal in  $x$ ,  $y$  and  $z$  directions ( $\theta_x$ ,  $\theta_y$  and  $\theta_z$ , respectively). The solid black line, in the upper panel, shows the iron formation.

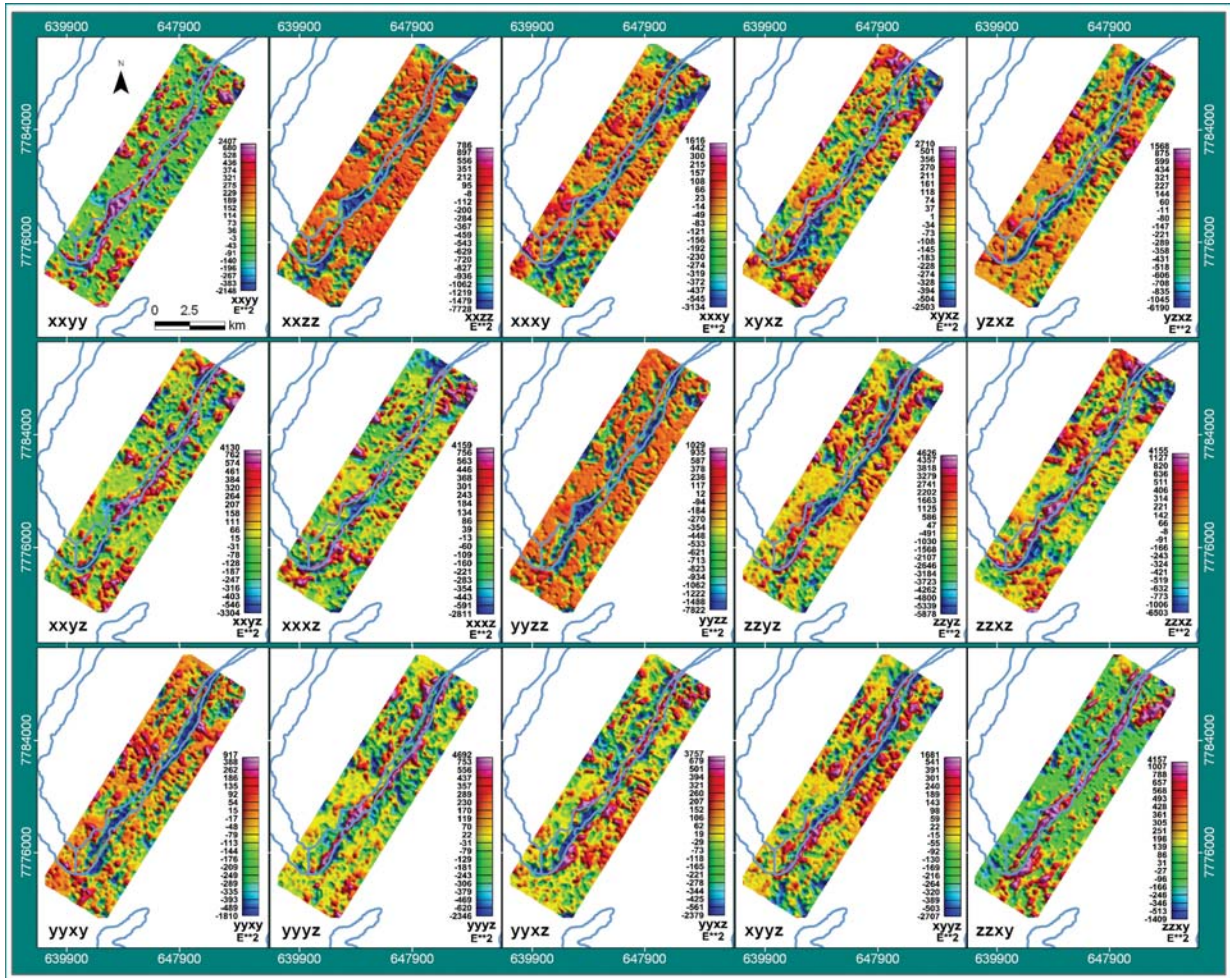


Figure 22 – Combination of two components of the gravity gradiometer tensor applied to the airborne survey data of Boa 6. The blue line represents the iron formation.

Figure 23 shows, three by three the simple combination of the six components of the gravity gradiometer tensor. Among the key results the combination  $xxyyzz$  displays results similar to  $I_2$  and few results are likely related to the mapping of areas of higher density contrast such as  $xxyyxy$ . Regarding the mapping of the geometry of the iron formation the combinations  $zzxyyz$  and  $xxzzyz$  display a good match.

Figure 24 shows four simple combinations, four by four. It is noteworthy that for the synthetic model combined four by four, only the patterns  $xxyyzzyz$  and  $xxyyzzxz$  indicate the direction of any geological feature of interest (see Fig. 13). In this area, the combinations that could correspond with the geology of the area would be:  $xxyyzzxy$  and  $yyzzxyyz$ .

Figure 25 shows a simple combination of components, five by five. In the right corner of the figure is shown a combination of all components. Only the combinations  $xxyyzzxyyz$

and  $xxyyzzxyxz$  are consistent with the geometry of the iron formation. The combinations of all components are not consistent (or show little correlation) with the geology of the area.

Finally, Figure 26 shows the modified determinant for two gradiometer systems: 3D-FTG and Falcon system. Note that apparently they show similar results and the figure of the digital terrain model with a resolution of 1 m was presented in the same figure for comparison. The 3D-FTG system is more sensitive to high-frequency mapping anomalies, such as the geological structure located in the northern part of the region. The Falcon system mapped features that were not evident in the processing of the 3D-FTG system; however, a careful analysis of systems to be used is recommended, taking into account parameters such as dimension of targets of interest, depth, etc. The analysis performed in this specific area suggests that the two systems produce results that are equivalent or complementary.

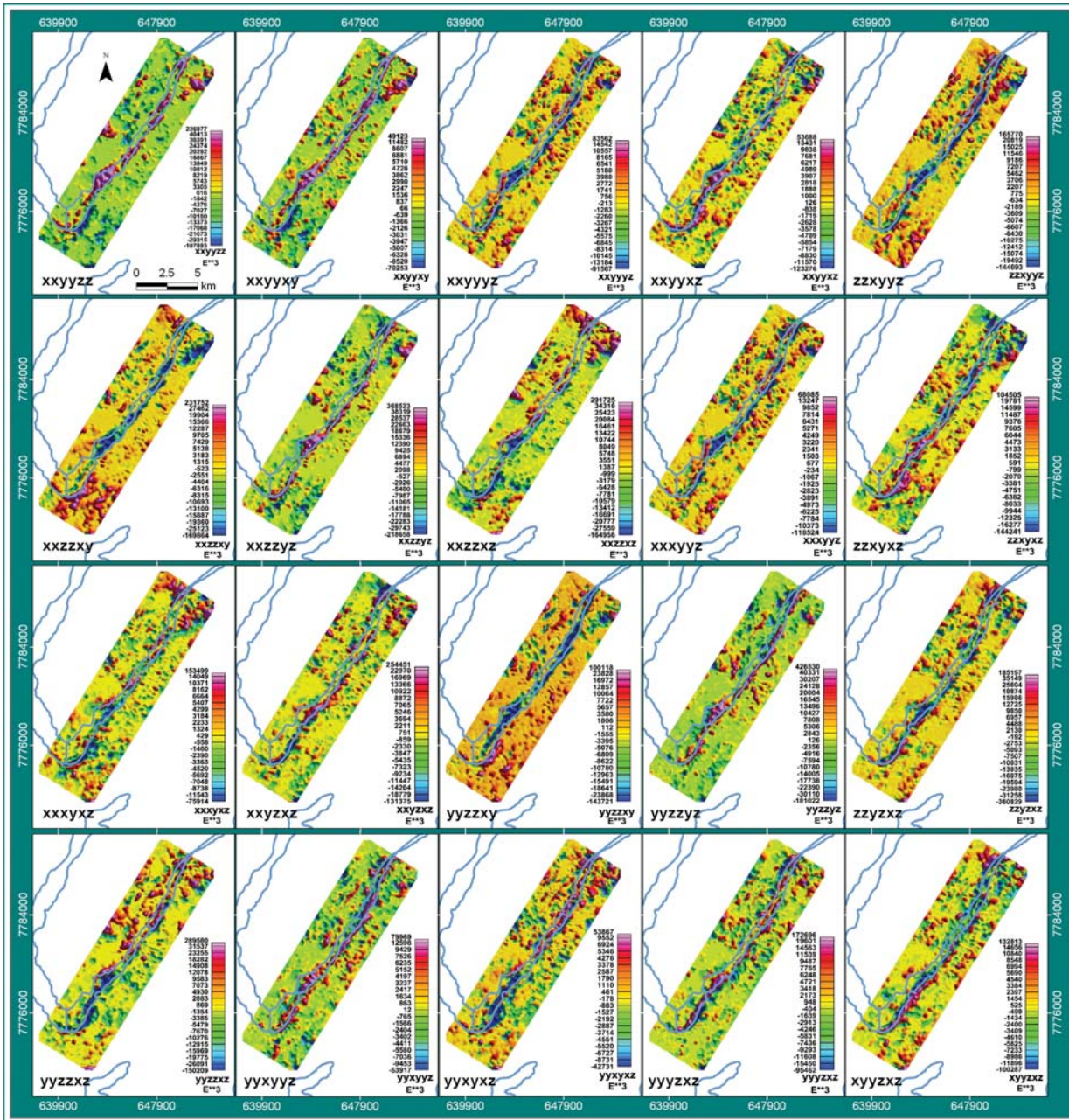
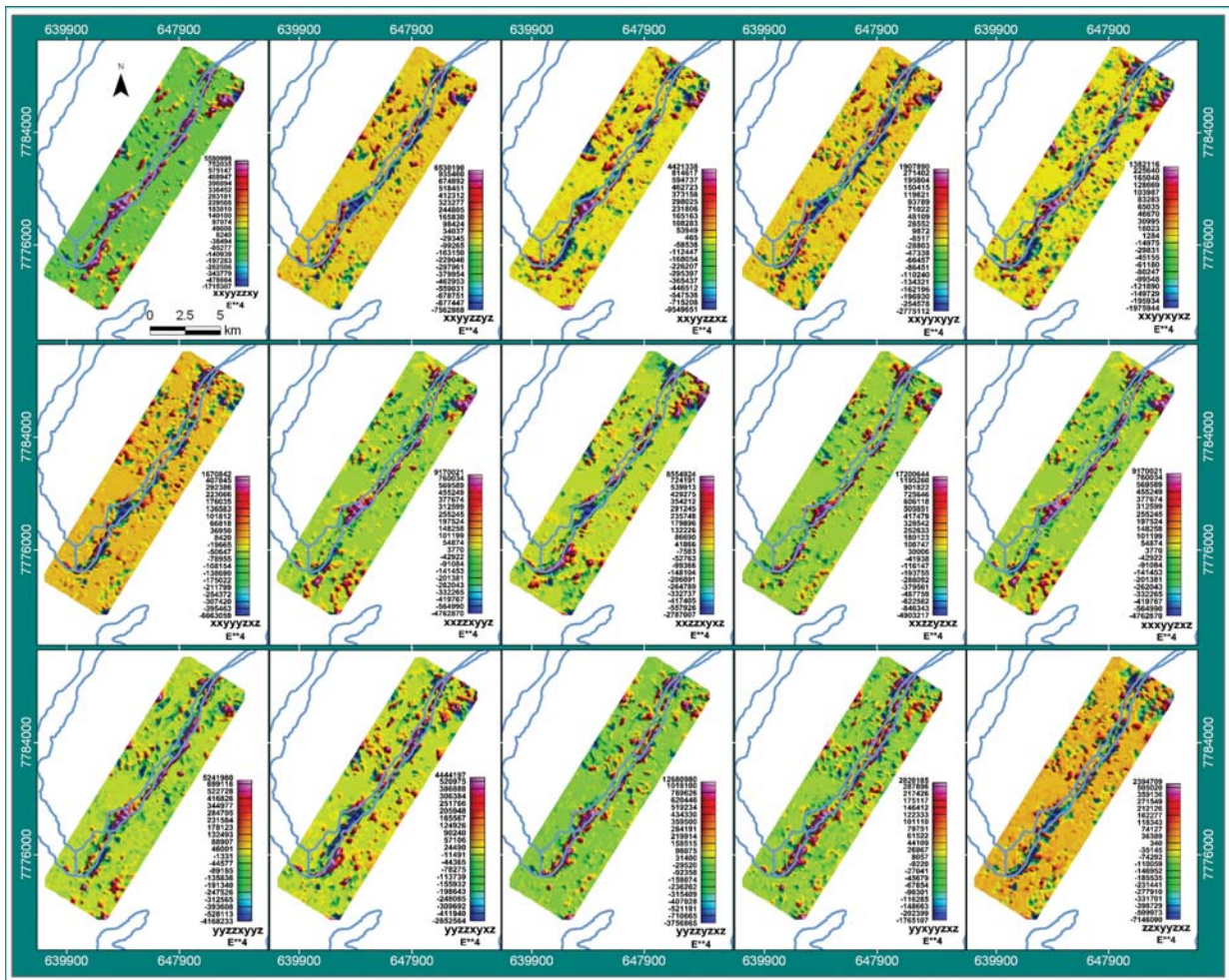


Figure 23 – Combination of the three components of the gravity gradiometer tensor applied to the airborne survey data of the Boa 6 area. The solid blue line represents the iron formation.

**ANALYSIS OF RESULTS/RECOMMENDATIONS**

Different methodologies were applied to process airborne gravity gradiometer data and a degree of equivalence could be observed in the results of different methodologies. The comparison of all these methodologies, which does not exist in the literature for a single article, provides a detailed analysis of the operation of each process, as well as their possible interactions

and applicability to each characteristic geological environment. The experimental combinations or simple combinations are excellent tools when a quick analysis of a prospective project is desired, giving a dynamic character to the procedures of analysis; however, it should not replace the standard procedures such as the calculation of invariants and eigenvalues for quite some time presented in the literature and recognized by the wide application in industry. Among the range of methods available for



**Figure 24** – Combination of four components of the gravimetric gradiometer tensor applied to the aerial survey data of Boa 6. The solid blue line represents the iron formation.

processing of gravity gradiometer data there are also other possibilities to define targets, also relevant, such as the use of the directional analytic signal and the curvature amplitude derived from the torsion balance.

Considering the feasibility of applying the methodologies in the outlining of lithological boundaries as in example Boa 6 area, a possibility that should be considered is the use of the results presented as *a priori* information for the preparation of geophysical inversion. The results can be used to validate either the obtained inverse model or the building of new geological models.

Once the requirements related to the potential applicability of the methods in exploration activities and their investigation resolution are met, the use of one or more of these techniques will depend exclusively on the complexity of the area being studied. In areas of relatively simple geology the application of two of the presented techniques would be enough to provide a view of the

geological setting and dimensions of the target and the consequent possibility of exploration. In areas such as Quadrilátero Ferrífero, applying all these techniques provide relevant and complementary information to the standard geological model of the area.

**CONCLUSION**

The results achieved through the application of various techniques presented in this article are consistent with the geology of the area, and aid in the decision-making process regarding to allocation of geological drilling for this region.

The assessment of capability of the method preceding the application to real geological situation, through the development of a synthetic model, is a practice of great value to establish a comparative parameter, enabling to project expected results to apply in real geophysical data. The results of all techniques were analyzed

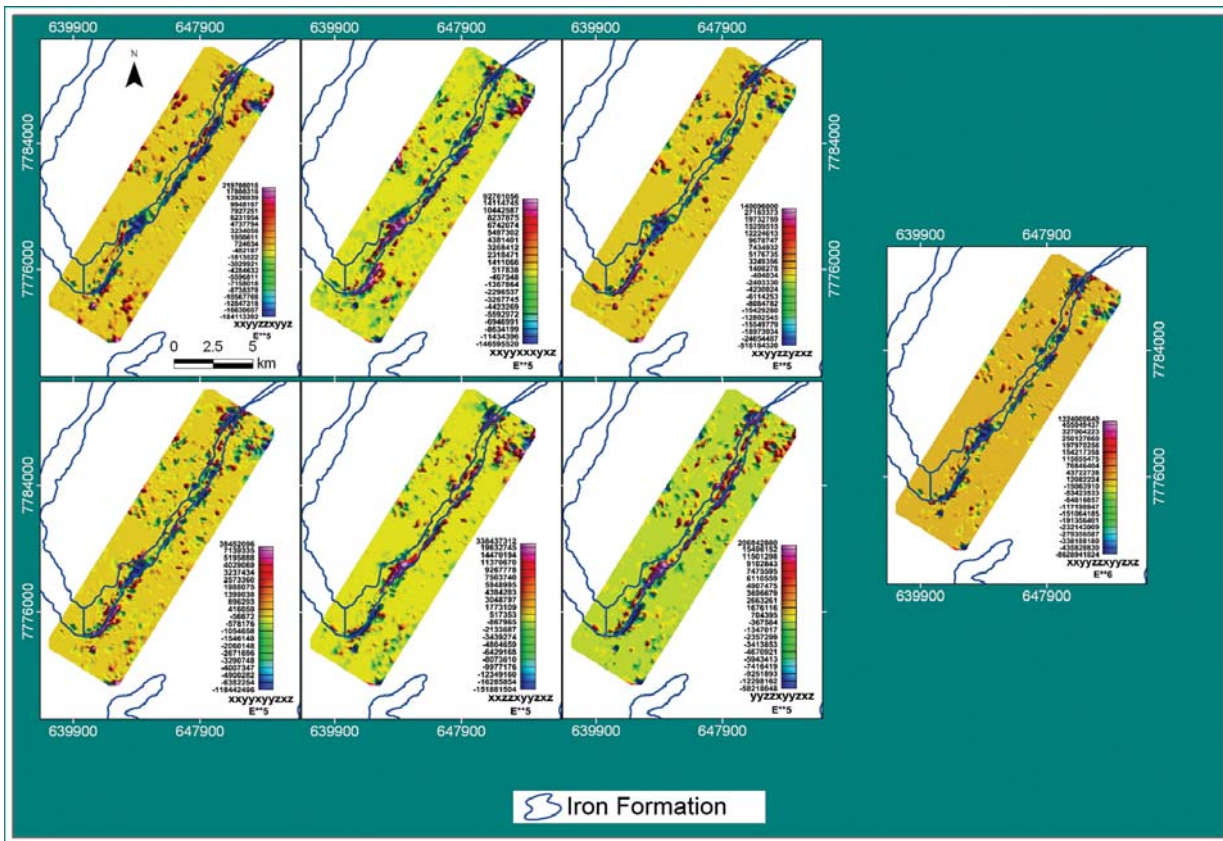


Figure 25 – Simple combination of five and six components (isolated figure) of the gravity gradiometer tensor for the airborne survey data of the Boa 6 area. The solid blue line represents the iron formation.

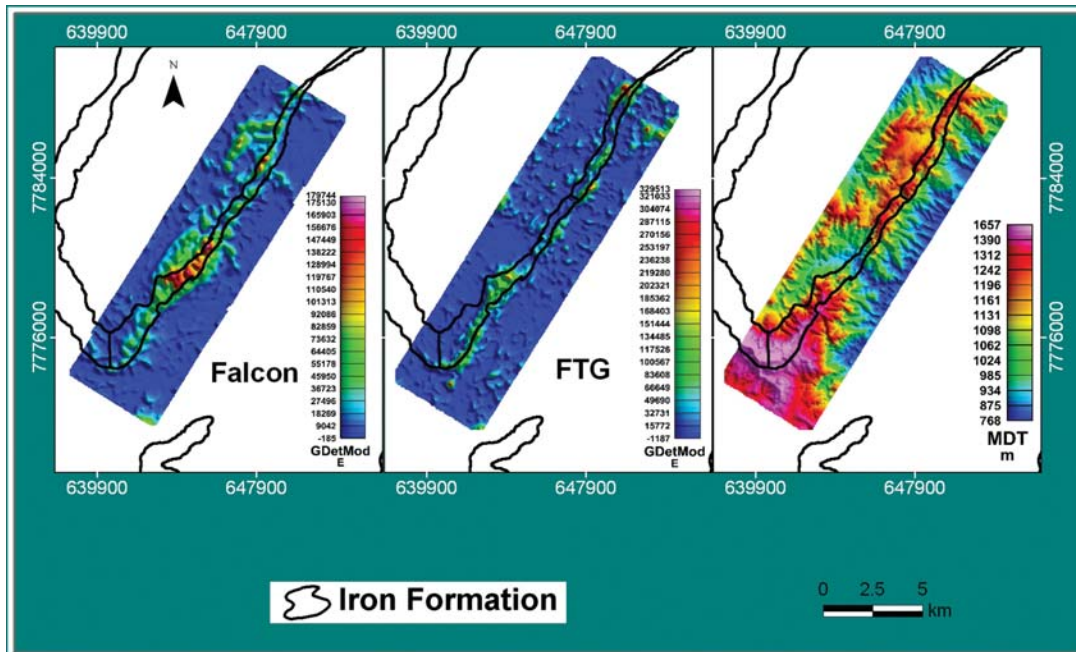


Figure 26 – Modified determinant ( $I_{detmod}$ ) for Falcon and 3D-FTG systems. The solid black line represents the iron formation.

together and many of them were considered equivalent within the application context for which they are intended as part of this article. The computer codes, developed by the authors, were all open source software. All routines have been tested and verified with the original studies, being viable to conduct the processing flows.

## ACKNOWLEDGMENTS

The authors thank VALE S.A. for granting permission to use the 3D-FTG and Falcon data and Mohamed Abdulla for the abstract corrections. D.U.C. is grateful to Vanderlei Coelho Oliveira Junior for the suggestion regarding the synthetic model; Leonardo Uieda, for his help with the open source software; and, the director of Vale S.A., Lucio Cavalli for the opportunity to perform doctorate studies at the National Observatory/Colorado School of Mines. The authors also thank two anonymous reviewers for corrections and suggestions presented to the work and Rodrigo Sousa Rocha for his support in GIS environment.

## REFERENCES

- AMES CB, FORWARD RL, LAHUE PM, PETERSON RW & ROUSE DW. 1973. Prototype Moving-Base Gravity Gradiometer, AFCRL-73-TR-73-0141. Hughes Research Laboratories, Malibu, California.
- BEIKI M. 2010. Analytic signals of gravity gradient tensor and their application to estimate source location. *Geophysics*, 75(6): 159–174, DOI: 10.1190/1.3493639.
- BEIKI M & PEDERSEN LB. 2010. Eigenvector analysis of gravity gradient tensor to locate geologic bodies. *Geophysics*, 75(6): 137–149, DOI: 10.1190/1.3484098.
- BEIKI M, PEDERSEN LB & NAZI H. 2011. Interpretation of aeromagnetic data using eigenvector analysis of pseudogravity gradient tensor. *Geophysics*, 76(3): L1–L10, DOI: 10.1190/1.3555343.
- BELL CC. 1971. Gravity Gradient Study. Hughes Research Laboratories. Final Report. Contract NAS-8-24788. Malibu, California, USA.
- BELL GEOSPACE. 2005. Final Report Acquisition and Processing Air-FTG Survey, Quadrilátero Ferrífero and Carajás Regions, Brazil.
- BRAGA MAS. 2009. Aplicação de Aerogravimetria Gravimétrica 3D-FTG na Prospecção de Minério de Ferro no Quadrilátero Ferrífero (MG) e Modelagem 2D e 3D para Estimativa de Massa do Depósito de Ferro de N1 em Carajás (PA). Doctorate Thesis, Universidade Federal do Rio de Janeiro. 271 pp.
- BRAGA MA, CARLOS DU, LI Y & NABIGHIAN M. 2010. Exploração de Minério de Ferro Utilizando Dados de Aerogravimetria Gravimétrica 3D-FTG e Aeromagnetometria no Quadrilátero Ferrífero, Minas Gerais, Brasil. *Revista Brasileira de Geofísica*, 28(3): 495–514.
- BRETT J. 2008. Theory of FTG measurements. [Online]. Available on: [http://www.bellgeo.com/tech/tecnology\\_theory\\_of\\_FTG.html](http://www.bellgeo.com/tech/tecnology_theory_of_FTG.html). Access on: Set. 12, 2011.
- BRETT J & BREWSTER J. 2010. Accelerometer and Rate Sensor Package for Gravity Gradiometer Instruments. U.S. Patent 7,788,975 B2.
- BRZEZOWSKI SJ, GOLDSTEIN JD, HELLER WG, TAYLOR TH & WHITE JV. 1990. Recent test results for gravity gradiometer survey system rail data: In: 7th Ann. Gravity Gradiometer Conf., Proceedings... GL-TR-90-0067, ADA223568, Geophysics Laboratory, Air Force System Command, Hanscom Air Force Base. 65–118 p.
- CARLOS DU, UIEDA L, BARBOSA VCF, BRAGA MA & GOMES Jr AAS. 2011. In-depth imaging of an iron orebody from Quadrilátero Ferrífero using 3D gravity gradient inversion. In: 81st Annual International Meeting. Expanded Abstracts, Society of Exploration Geophysicists, 902–906.
- CORDELL L & GROUCH VSJ. 1985. Mapping basement magnetization zones from aeromagnetic data in the San Juan basin, New Mexico. In: HINZE WJ (Ed.), *The utility of regional gravity and magnetic anomaly maps*. SEG, 181–197.
- DICKINSON JL, MURPHY CA & ROBINSON JW. 2010. FTG Data Imaging Techniques for Geological Interpretation In: ASEG Extended Abstracts, 1, 1–4.
- DRANSFIELD MH. 1994. Airborne gravity gradiometry. PhD. Thesis, University of Western Australia. 254 pp.
- DRANSFIELD MH, CHRISTENSEN A, ROSE M, STONE P & DIORIO P. 2001. "FALCON test results from Bathurst mining camp". *Exploration Geophysics*, 32: 243–246.
- DRANSFIELD MH. 2007. Airborne Gravity Gradiometry in the Search for Mineral Deposits. In: Fifth Decennial International Conference on Mineral Exploration. Proceedings of Exploration 07, 341–354.
- DRANSFIELD MH & GAMMA F. 2010. Processamento de Dados Gravitométricos Gravimétricos do Sistema FALCON (AGG). *Boletim da Sociedade Brasileira de Geofísica*, 4: ISSN: 2177–9090
- FITZGERALD DJ & HOLSTEIN H. 2005. Innovative Data Processing Methods for Gradient Airborne Geophysical Datasets. In: Proceedings... SAGA 2005. 10 pp.
- FITZGERALD D & HOLSTEIN H. 2006. Innovative data processing methods for gradient airborne geophysical datasets. *The Leading Edge*, 25: 87–94, DOI: 10.1190/1.2164762.
- FORWARD RL. 1981. Gravity Sensors and the Principle of Equivalence. *IEEE Transactions of Aerospace and Electronic Systems*, 17: 511–519.
- GALBIATTI H, BRAGA MA, CARLOS DU & SOUSA RR. 2011. 3D-FTG and Falcon Airborne Gravity Gradiometer Systems for Iron Ore Exploration. *Revista Brasileira de Geofísica*, 29(4): 801–810.
- HEATH P. 2007. Analysis of Potential Field Gradient Tensor Data: Forward Modelling, Inversion and Near-Surface Exploration. School of

- Chemistry and Physics. PhD thesis: University of Adelaide, Australia. 206 pp.
- HOPKINS J. 1975. Gravity Gradiometry – A Rebirth. Defense Mapping Agency, Aerospace Center, St Louis, AFS, Missouri.
- JEKELI C. 1988. The gravity gradiometer survey system (GGSS). *Eos*, 69: 105–117.
- JEKELI C. 1993. A review of gravity gradiometer survey system data analyses. *Geophysics*, 4: 508–514.
- JEKELI C. 2006. Airborne Gradiometry Error Analysis. *Surveys in Geophysics*, 27: 257–275.
- LANE R.J.L. 2004. Integration ground and airborne data into regional gravity compilations. In: Abstracts from the ASEG-PESA Airborne Gravity Workshop. *Geoscience Australia Record*, 81–97.
- MATARAGIO J & KIELEY J. 2009. Application of full tensor gradient invariants in detection of intrusion-hosted sulphide mineralization: implications for deposition mechanisms. *First Break*, 27: 95–98.
- MATARAGIO J, JORGENSEN G, CARLOS DU & BRAGA MA. 2011. State of Art Techniques for iron Oxide Exploration. In: 12th International Congress of the Brazilian Geophysical Society. CD-ROM.
- METZGER EH. 1974. Overview, Rotating Accelerometer Gradiometer for Correcting Inertial Navigation Systems for the Deflection of the Vertical; Bell Aerospace Company; Buffalo, New York.
- METZGER EH. 1977. Recent gravity gradiometer developments. In: GARG S, MORROW L & MANEN R (Ed.), Guidance and Control Conference, Hollywood, Fla., August 8-10, 1977. Technical Papers. (A77-42751 2-35) New York, American Institute of Aeronautics, Inc., 306-315.
- METZGER EH. 1986. Development Experience of a Moving Base Gravity Gradiometer and Discussion of Future Applications; Bell Aerospace Textron; Buffalo, New York.
- MILLER HG & SINGH V. 1994. Potential field tilt – A New concept for location of potential field sources. *Journal Applied Geophysics*, 32: 213–214.
- MURPH CA. 2004. The Air-FTG Airborne Gravity Gradiometer System. In: LANE R (Ed.), Airborne Gravity 2004 Workshop, *Geoscience Australia Record*, 2004/18, 7–14.
- MURPH CA. 2007. Interpretating FTG Gravity Data using Horizontal Tensor Components. In: EGM 2007 International Workshop. Innovation in EM, Grav and Mag Methods: a new Perspective for Exploration.
- MURPHY CA & BREWSTER J. 2007. Target delineation using full tensor gravity gradiometry data. In: ASEG Extend Abstract 2007 (1), 1–3.
- NABIGHIAN MN. 1984. Toward a three-dimensional automatic interpretation of potential field data via generalized Hilbert transforms – Fundamental relations. *Geophysics*, 49: 780–786, DOI: 10.1190/1.1441706.
- NAGY D, PAPP G & BENEDEK J. 2000. The gravitational potential and its derivatives for the prism. *Journal of Geodesy*, 74: 552–560.
- NAGY D, PAPP G & BENEDEK J. 2001. Corrections to “The gravitational potential and its derivatives for the prism”. *Journal of Geodesy*, 76: 475, DOI: 10.1007/s00190-002-02264-7.
- O'KEEFE GJ, LEE JB, TURNER RJ, ADAMS GJ & GOODWIN GC. 1999. Gravity Gradiometer. U.S. Patent 5,922,951.
- ORUÇ B & KESKINSEZER A. 2008. Structural Setting of the Northeastern Biga Peninsula (Turkey) from Tilt Derivatives of Gravity Gradient Tensors and Magnitude of Horizontal Gravity Components. *Pure and Applied Geophysics*, 165: 1913–1927.
- PEDERSEN LB & RASMUSSEN TM. 1990. The gradient tensor of potential field anomalies. Some implications on data collection and data processing of maps. *Geophysics*, 55(12): 1558–1566.
- PFOHL L, RUSNAK W, JIRCITANO A & GRIERSON A. 1988. Moving-base gravity gradiometer survey system (GGSS) program. Final Report, Mar 1983 – Apr. 1988. Textron Bell Aerospace Co., Buffalo, NY.
- ROEST WR, VERHOEF J & PILKINGTON M. 1992. Magnetic interpretation using the 3-D analytic signal. *Geophysics*, 57: 116–125, DOI: 10.1190/1.1443174.
- ROGERS MM. 2009. An Investigation into the Feasibility of Using Modern Gravity Gradient Instrument for Passive Aircraft Navigation and Terrain Avoidance. Department of Aeronautics and Astronautics, Air Force Institute of Technology, Wright-Patterson AFB, Mater's Thesis, 180 pp.
- TÓTH G. 2002. Prediction by Eotvos' Torsion Balance Data in Hungary. *Periodica Polytechnica Ser. Civ. Eng.*, 46(2): 221–229.
- TRAGESER MB. 1970. A Gradiometer for Gravity Anomaly Surveying, *Advances in Dynamic Gravimetry*, KATTNER WT (Ed.), Inst. Soc. of America, 1-35.
- TRAGESER MB & JOHNSON DO. 1974. Preliminary Gravity Gradiometer System Definition Report; C-4196; The Charles Stark Draper Laboratory; Cambridge, Massachusetts.

---

## NOTES ABOUT THE AUTHORS

**Dionísio Uendro Carlos.** Bachelor and Master degrees in Geophysics at IAG/USP. Ph.D. in Geophysics at the Observatório Nacional/MCTI/Colorado School of Mines. Was a visiting researcher at the Geophysics Department, Colorado School of Mines (USA) and is, currently, Geophysics coordinator of the Ferrous Mineral Exploration at VALE.

**Marco Antonio Braga.** Ph.D. and Masters in Geology, with emphasis in Applied Geophysics from the Universidade Federal do Rio de Janeiro/Colorado School of Mines, in 2009. Specialized in geophysical methods applied to exploration of iron ore. Currently, is the manager of the Ferrous Mineral Exploration at VALE.

**Henry F. Galbiatti.** Master in Structural Geology and Geotechnical Engineering from the Universidade Federal de Ouro Preto. Currently, is the general manager of Ferrous Mineral Exploration and Integrated Management at VALE.

**Wanderson Roberto Pereira.** Graduated in Geophysics from the IAG/USP. Currently, works at VALE in management of Ferrous Mineral Exploration. Develops studies related to quality control, processing and interpretation of geophysical profiles of wells applied to Ferrous Mineral Exploration.